Combined Optical Trapping and Single Molecule Fluorescence to Study the Force-dependent Binding Kinetics between Filamentous Actin and its Partners

by

Jorge M. Ferrer
B.S. Mechanical Engineering
University of Puerto Rico, 1999

Submitted to the Department of Mechanical Engineering in Partial Fulfillment of the Requirements for the Degree of

Master of Science in Mechanical Engineering
at the
Massachusetts Institute of Technology

June 2004

Signature redacted

Signature of Author.....
Department of Mechanical Engineering
May 7, 2004

Signature redacted

Certified by .....
Roger D. Kamm
Professor of Mechanical Engineering Department
Thesis Supervisor

Signature redacted

Certified by .....
Matthew J. Lang
Assistant Professor of Mechanical Engineering Department
Thesis Supervisor

Signature redacted

Accepted by .....
Ain Sonin
Professor of Mechanical Engineering
Chairman, Committee for Graduate Students

Combined Optical Trapping and Single Molecule Fluorescence to Study the Force-dependent Binding Kinetics between Filamentous Actin and its Partners

by

Jorge M. Ferrer

Submitted to the Department of Mechanical Engineering on May 7, 2004 in Partial Fulfillment of the Requirements for the Degree of Master of Science in Mechanical Engineering

Abstract

Actin filaments are a major constituent of the cytoskeleton in most eukaryotic cells. They function as a connection between the cell body to the focal adhesions in order to transmit forces into and out of the cell. During the force transduction process, many proteins bind to actin filaments in order to initiate a signaling cascade that reaches the cell nucleus. However, the effects of forces in the binding kinetics between actin filaments and actin binding proteins are unknown. This work proposes an experimental setup to study the force-dependent binding kinetics of such proteins at the single molecule level by using an instrument that combines optical trapping with single molecule fluorescence.

The main focus of this work was the design and construction of the experimental equipment. The results show position detection capabilities with a resolution of 5 nm. Also, the trap stiffness recorded was in the order of 0.05 pN/nm. With the combination of position and trap stiffness, the force resolution of the instrument is about 0.25 pN. Also, a photobleaching event for a single dye molecule was recorded, proving the single molecule fluorescence capabilities.

In addition, a complete experimental assay is described in order to perform studies on how force application affects the binding of actin and actin binding proteins.

Thesis Supervisor: Roger D. Kamm
Title: Professor of Mechanical Engineering Department

Thesis Supervisor: Matthew J. Lang
Title: Assistant Professor of Mechanical Engineering Department

Table of Contents

List of Figures

List of Tables

Chapter 1: Introduction

Mechanical forces play a critical role in cell cycle and survival. External forces from the surroundings and internal forces affect cell morphology, orientation, migration, adhesion and can even induce apoptosis. For example, when a monolayer of endothelial cells is subjected to fluid shear, the morphology of the cell changes from a polygonal shape into a more elongated shape aligned with the direction of fluid flow [2, 3]. During actin-based cell migration, actin filaments polymerize at the leading edge generating forces that protrude the cell membrane in the direction of motion [4-8]. When adhered to a substrate, the cell probes the stiffness of the matrix by transmitting internal forces from the combination of the motor protein myosin and actin stress fibers through the focal adhesions, in order to determine in which direction the matrix is stiffer and eventually migrate in that direction [9]. In each of these studies, it was shown that in eukaryotic cells forces are transmitted throughout the cell body by actin filaments forming the cytoskeletal network, stress fibers, and focal adhesion linkages. Therefore, understanding the relationship between actin mechanics and cellular responses is important in order to provide insight in the process of force transduction into a cellular bio-chemical reaction. This process is known as mechanotransduction.

At force transmission sites, multiple proteins are recruited to link the extracellular matrix to the cell. Several extracellular proteins, including fribronectin and vitronectin, adhere to the extracellular domain of the transmembrane protein integrin. The intracellular domain of integrin is linked to the actin cytoskeleton by means of multiple protein-protein interactions including vinculin, talin, filamin, paxillin, focal adhesion kinase (FAK), α-actinin and fimbrin among others [10], and they are part of the force signaling cascade into the cell nucleus. Some of these proteins are also actin-binding proteins (ABP). The overall goal of this work is to understand how the binding kinetics of actin binding proteins is affected by actin mechanics as the filament is loaded with tensile force. In general, force application can change the interaction energetics between two proteins; therefore, a different conformational state may become more favorable. The approach presented here is to study these binding reactions at the molecular level between a single actin filament and a single ABP molecule *in vitro*. In order to perform

single molecule experiments, an instrument capable of applying forces while simultaneously monitoring molecular events is required. Previously, optical trapping combined with single molecule fluorescence has been shown to fulfill these requirements [1]. Therefore, the primary focus of this work is to describe the design, development and capabilities of such equipment, and present how this instrument will be used in experimental procedures.

Optical trapping as well as fluorescence microscopy are techniques that have been utilized by researchers in different areas for some time. Although these two methods are not new, the combination of both in one instrument has been a challenge until recent developments [1]. The design of the instrument presented here is based on a previous instrument [1] but with several modifications to add more capabilities and improved performance.

In the next section, a summary of the function of F-actin is presented, followed by an overview of the history and theory behind optical trapping and single molecule fluorescence. In chapter 2, the design of the equipments as well as capabilities is described. This is followed by the experimental methods (chapter 3) where equipment calibrations are described and the initial biological assays preparation is presented. The results of these methods are presented in chapter 4. This chapter also includes theoretical results to determine experimental quantities to be used, as well as a simulation of data analysis to obtain the dissociation constant between ABP's and F-actin under different loads. In chapter 5, the results are discussed in detail. The work finalizes with a brief presentation of future directions and conclusions (chapter 6).

1.1.1 Actin and actin binding proteins

Actin is a cytoskeletal protein consisting of 631 amino acid residues, with a molecular weight of 43 kDa. The actin molecule (G-actin) is divided into four sub-domains with a nucleotide-binding cleft at the center of the molecule. Generally, under physiological conditions, actin is present in two distinct forms: ADP-bound or ATP-bound, which retards or promotes actin polymerization, respectively. Inside a living cell, actin is present in its monomeric form or in the fibrous polymer form (frequently called filamentous actin or F-actin). Filamentous actin is grown by the sequential polymerization of monomers in the ATP-bound state, forming a two-stranded helical

polymer, when local concentrations of cations (Mg^{2+}, Ca^{2+}) are high. For example, in pure water, only G-actin is present, but in solution with physiological salt concentrations, only F-actin would be present [11]. Once in filament form, the ATP in the G-actin is hydrolyzed; therefore, most of the filament consists of GDP-actin. Although it has been observed that polymerization can occur with GDP-actin, the rate of polymerization is much slower than with ATP-actin [11]. The actin filament has a polarized structure: the barbed end and the pointed end. This nomenclature was given to each end of the filament because its physical appearance under electron microscopy imaging. Observations of polymerization process have shown that the barbed end is the fastest growing end. Actin filaments form either heavily branched networks or dense bundles depending on the proteins that bind to them. F-actin networks are the primary component of the cytoskeleton, providing structural integrity to the cell. On the other hand, bundles of filaments form stress fibers that increases cell rigidity in a particular directions. Some of these bundles are like stiff rods on which myosin motors pull in order to contract the cell during migration. Hence, actin filaments play multiple roles throughout the cell contributing to cell adhesion, migration and survival.

Inside the cell, the distribution between monomeric and filamentous forms of actin is regulated by the local concentration of both as well as the presence of capping, severing and sequestering proteins (Table 1.1). At the leading edge, conditions favor the formation of filaments in order to form protrusions (lamellipodia) that initiate cell migration. At focal adhesions, conditions keep a stable filament to provide a solid anchor and transmit forces along the cell. Previous work [12] has shown an increase in activation of several proteins at the focal adhesion site when the cell is mechanically stretched, but no quantitative data are available to describe how the binding kinetics are affected. As part of this work, an experimental method to quantify the binding kinetics between actin-binding proteins and actin filaments as tensile forces are applied to the filament is presented. The premise behind these studies is that application of force can change the energetics of some reactions, shifting the system to a different conformation. This conformation could result in a higher or lower binding affinity, which is what the goal of this project is aimed to study. The results of future experiments can elucidate which proteins are more active under force application. These could provide a better

understanding of the signaling cascade that transforms a mechanical stimulus into a bio-chemical reaction.

Protein name	*Molecular Weight*	*Function*
α-actinin	100 kDa	F-actin crosslinker, promotes bundles or network
Vinculin	124 kDa	Stabilizes interaction between talin and actin, and talin and lipid bilayer
Talin	270 kDa	Couples membrane proteins with cytoskeletal proteins
Filamin	280 kDa	F-Actin crosslinker, promotes actin networks
Fimbrin	68 kDa	F-actin crosslinker, promotes bundling
Gelsolin	86 kDa	F-actin severing and capping protein
Arp2/3	45 kDa	Promotes filament branching
ADF/cofilin	19 kDa	Promotes actin depolymerization
VASP	40 kDa	Promotes polymerization, inhibits barbed end capping
Fascin	55-58 kDa	F-actin crosslinker, promotes bundling

Table 1.1. Actin binding proteins, molecular weights (approximate) and functions

1.1.2 Optical Trapping

History

The concept of force generated by an incident beam of light on a surface has been studied since the seventeenth century. During that time, based on astronomical observations, the German astronomer Johannes Kepler hypothesized that the reason for the comet tails to point away from the sun was because the sun's radiation pushes them in that direction. Although this idea was considered extreme by that era, it set the stage for what was later known as the phenomenon of radiation pressure. In the late nineteen hundreds, James Maxwell, with his Theory of Electromagnetism, showed mathematically that light incident on a surface can actually generate a force, namely radiation pressure. The first experimental evidence of radiation pressure was obtained in 1901 by the Russian Pyotr Nikolaievich Lebedev [13] and by (unrelated experiments) the Americans Ernest Fox Nichols and Gordon Hull [14]. While their experiments were fairly simple (a light beam incident on a glass surface suspended in air by a fine torsional fiber), their results are the basis for the widely used technique of optical tweezers.

With the introduction of lasers during the 1960's, scientists found a way to generate a relatively small diameter beam with very high intensity. These high intensity laser beams can be focused to a tight, diffraction-limited spot that can generate forces to push, pull or

trap small objects with sizes ranging from a few to tens of micrometers depending on their optical properties. These observations prompted Arthur Ashkin [15-18] to perform pioneering experiments on optical tweezers. By 1986, Ashkin *et al* [19] demonstrated the first optical tweezers application by using a microscope objective to tightly focus a laser beam, attaining a stable three-dimensional trap. A year later Ashkin and others [20, 21] demonstrated several biological applications of optical tweezers by trapping bacteria, viruses and yeasts. These accomplishments initiated a technological revolution in manipulation of micron-sized particles that led to the sophisticated equipment used in optical tweezers.

Handles in optical tweezers

In biological applications, trapping the specimen is usually difficult because specimens usually have non-uniform geometry and/or optical properties. For this reason, the technique of using optical handles has been adopted. These handles are tethered to the specimen by means of protein-protein interactions. The most common types of handles are polystyrene and silica microspheres and they can be found commercially in a wide range of sizes and surface chemistry. These types of handles have much better optical properties than biological specimens, which enhance the trapping forces as well as trap stability.

Current applications

Optical tweezers have found widespread applications in the biological world. By using a near infrared laser, minimal damage to the biological specimen is obtained, as well as leaving the visible spectrum open for fluorescence microscopy. Current experiments range from probing mechanical properties of the cell, down to measuring single molecule events. In the future optical tweezers can be introduced in the nano-fabrication technology for its versatility and precise position control.

Applications in cell biology include studies in red blood deformation [22, 23], cell locomotion and lamellipodia formation [24, 25], focal adhesion formation [26], as well as manipulating single cells such as sperm, bacteria and viruses [20, 21, 27]. Optical traps are used in these applications since they provide a non-invasive method of probing cell characteristics.

At the molecular level, energy states are measured in terms of the thermal energy of a particle, which is expressed as k_BT, where k_B is the Boltzmann constant (1.38×10^{-23} J/K) and T is the absolute temperature. At room temperature, thermal fluctuations have an energy of $k_BT \sim 4 \times 10^{-21}$ J or 4 pN·nm. In these force and length scales optical traps have a suitable application since they can usually apply forces in the range of 100 pN, and many protein conformational changes are just a few nanometers in range; therefore, the energy of the trap (~ 500 pN·nm) dominates the thermal fluctuation energy. In this area, extensive work have been done on DNA stretching [28, 29] and unzipping [1]. Also, other studies include the mechanics of molecular motors such as kinesin [30-32] and myosin [33-35]. Results show that optical tweezers are an excellent tool for recording events at the single molecule level. For this reason, this tool was selected as the experimental equipment to study force dependent binding between actin filaments and actin binding proteins.

Optical trapping theory

As mentioned above, optical tweezers generate trapping forces by means of radiation pressure. When a laser beam passes through a dielectric particle several forces are generated but the two most important are the scattering force and the gradient force [36]. The scattering force acts in the direction of propagation of the beam, and is proportional to the intensity of the incident beam. On the other hand, the gradient force is proportional to the spatial distribution of intensity of the beam and acts in the direction towards the higher intensity region. Since these two forces have components that act against each other, a force balance between them is required to obtain a stable optical trap.

The theoretical description of the forces acting on a particle can be catalogued in to three regimes: (1) object dimension much greater than the wavelength of light ($d \gg \lambda$) or Mie regime, (2) object dimension comparable to wavelength ($d \approx \lambda$), and (3) object dimension much smaller than the wavelength ($d \ll \lambda$) or Rayleigh regime. In the Mie regime, particle trapping can be described using ray optics because the diffraction limited focus size is much smaller than the particle dimension. In the Rayleigh regime, particles can be represented as point dipoles and electromagnetic theory is required to describe the trapping phenomenon [36]. When the dimensions of the particle and the wavelength are comparable, all the dimensions involved are important, making it very difficult to

describe theoretically how the forces are generated. Unfortunately, this regime includes biological applications, where the characteristic size is ~ 1μm and the laser wavelength used is around 1064nm. At this wavelength cells and tissues exhibit very low absorption of light and minimal damage to the specimen is obtained. In this case, theoretical description of the optical trap is lagging behind experimental methods, and since favorable experimental results have been obtained, it seems that not much attention has been paid to the theory [37]. In the following paragraphs, a description of optical trapping in the Mie and Rayleigh regimes are presented.

Mie regime

In this regime, geometrical (or ray) optics provides a good approximation to describe the trapping force generation. When a ray of light passes through a refractive medium, such as a dielectric microsphere, it is bent while entering and exiting the particle (Figure 1.1). The momentum of the light is changed at each bend, and by conservation of momentum of the system, the momentum of the particle has to change by the same magnitude but opposite direction. Using Newton's Second Law, the rate of change of momentum generates a force in the following way

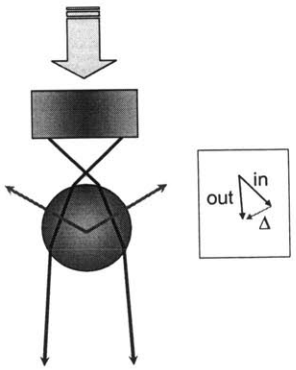

Figure 1.1. Ray optics representation of gradient forces in optical trap. The green arrows represent the net force generated by each ray. *Inset*: momentum change of the beam entering from the left of the particle.

$$\vec{\mathbf{F}}_{grad} = \frac{d\vec{\mathbf{p}}}{dt} \approx \frac{\Delta\vec{\mathbf{p}}}{\Delta t}. \qquad \text{Equation 1.1}$$

From Figure 1.1, the horizontal components of the force cancel out and the net force acts toward the focus of the beam. Equation 1.1 only describes the gradient force, and it can be seen that it acts in the same direction as the momentum change of the particle. Further analysis is needed to obtain the scattering force, and only the result will be shown here. Notice that the particle will be pulled towards the focus of the beam only if the index of refraction of the particle is greater than the index of refraction of the medium.

From Ashkin [18], in the Mie regime, the vector force $\vec{\mathbf{F}}$ imparted by a single ray is described by

$$\vec{\mathbf{F}} = \frac{n_m P}{c}\left\{1 + R\cos 2\theta - \frac{T^2\left[\sin(2\theta - 2\varepsilon) + R\cos 2\theta\right]}{1 + R^2 + 2R\cos 2\varepsilon}\right\}\hat{\mathbf{i}} + \frac{n_m P}{c}\left\{R\sin 2\theta - \frac{T^2\left[\sin(2\theta - 2\varepsilon) + R\cos 2\theta\right]}{1 + R^2 + 2R\cos 2\varepsilon}\right\}\hat{\mathbf{j}}, \quad \text{Equation 1.2}$$

where θ is the angle of incidence, ε is the angle of refraction, R and T are the Fresnel coefficients of reflection and transmittance respectively and $\hat{\mathbf{i}}$ and $\hat{\mathbf{j}}$ are the unit vectors in the direction parallel and perpendicular to the direction of the incident beam respectively. By definition the scattering force acts is the $\hat{\mathbf{i}}$ component and the gradient force is the $\hat{\mathbf{j}}$ component. Therefore, the $\hat{\mathbf{j}}$ component gives a better description of the momentum change presented in Eq. 2.1. The net force acting on a particle is given by the vector sum of all the rays of the incident beam.

Rayleigh regime

Radiation pressure is generally expressed as

$$\mathcal{P} = \frac{I}{c} \quad \text{Equation 1.3}$$

in terms of force per unit area where I is the intensity of the beam (power per unit area) and c is the speed of light, or in terms of force

$$F = \frac{P}{C} \quad \text{Equation 1.4}$$

where P is the power of the incident beam. When considering the index of refraction of the solution medium, the force (and pressure) equation becomes

$$F = \frac{Q n_m P}{c}, \quad \text{Equation 1.5}$$

where Q is a measure of the efficiency depending of type of beam (plane wave, spherical wave, mode, polarization and the optical properties of the particle), and n_m is the index of refraction of the medium.

In the Rayleigh regime, the electric field is considered uniform at the dielectric particle. Using this assumption, the scattering force is described as

$$\vec{\mathbf{F}}_{scatt} = \frac{n_m \langle \vec{\mathbf{S}} \rangle \sigma}{c}, \quad \text{Equation 1.6}$$

where $\langle \vec{\mathbf{S}} \rangle$ is the time-average Poynting vector and

$$\sigma = \frac{8}{3}\pi(ka)^4 a^2 \left(\frac{n_r^2 - 1}{n_r^2 + 2}\right)^2, \qquad \text{Equation 1.7}$$

is the scattering cross section of the Rayleigh sphere with radius a and index of refraction n, $n_r = n/n_m$ is the relative index, and $k = 2\pi n_m/\lambda$ is the wave number of the beam. Equation 2.6 shows that the scattering force acts in the direction of the propagating light. The gradient force is given by

$$\vec{\mathbf{F}}_{grad} = \frac{\alpha}{2}\nabla\langle E^2 \rangle, \qquad \text{Equation 1.8}$$

where

$$\alpha = n_m^2 \left(\frac{n_r^2 - 1}{n_r^2 + 2}\right)^2, \qquad \text{Equation 1.9}$$

is the polarizability of the particle and $\langle E^2 \rangle$ is the time-average of the dot product of the electric field [36].

The Mie and Rayleigh regimes provide a physical and mathematical model for how forces are generated to trap particles using laser beams. In practice, this theory is seldom used to determine the optical forces because experimental setups are quite complex and not all the optical properties of the specimens are characterized. Instead, optical forces are determined experimentally using different methods discussed section 3.1.

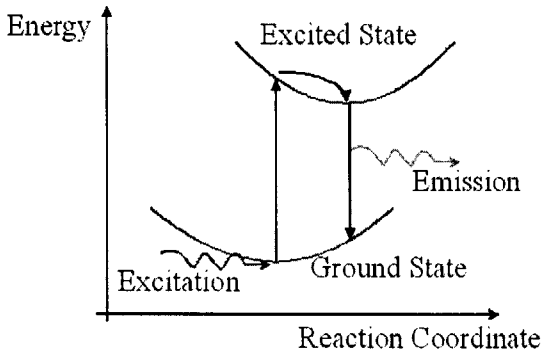

Figure 1.2. Excitation and emission of fluorescent dyes. When the excitation beam hits an electron at ground state, it jumps to the higher energy excited state. In order to return to its ground state, energy is released in form of light. Since there is some energy loss in the process, the emission wavelength is longer than the excitation wavelength; therefore, emission occurs at a different color.

1.1.3 Fluorescence Microscopy

Many studies in biology require tracking very small particles (~nm) and/or events that are not capable of being observed with a light microscope, even at high magnification. In general the smallest particle visible in a light microscope is on the order of the light source wavelength. For these cases, a particle can be labeled with a fluorescent dye that emits light when excited at a specific wavelength (Figure 1.2). By locating the center of the point spread function of the light emission, the position of the particle can be resolved even if the particle can not be visible because of it

size. This technique is called fluorescence microscopy. In this technique, a set of filters are used to block the excitation light from getting into the eye piece such that the image is generated only by the emission light from the dyes. The application of these fluorescent dyes is dictated by their properties of excitation and emission spectrum, and a wide selection of dyes is now available in the market to fit specific needs.

Although fluorescence microscopy has the advantage of being able to track particles at the nanometer and sub-nanometer range, this technique also has one disadvantage: a low signal-to-noise ratio (SNR). Since the whole specimen contains the fluorescent dyes, not only the region in the focal plane will get excited but also the rest of the solution in the laser path. This background fluorescence could decrease the ability of discerning between single events reducing the spatial resolution. A technique commonly used to reduce background effects is total internal reflection (TIR). With TIR, only a thin region of the specimen plane is excited by an evanescent wave, eliminating background fluorescence outside the focal plane. Total internal reflection fluorescence microscopy has made it possible for researchers to even record single molecule events [1, 36] that could not have been observed otherwise.

Principles of total internal reflection fluorescence microscopy (TIRFM)

When light travels from one medium to another, it can either get transmitted, reflected, absorbed or some combination of all of the above. To analyze this phenomenon, consider the case of an incident monochromatic plane wave with an electric field in the form of the complex exponential

$$\vec{\mathbf{E}}_i(\vec{\mathbf{r}},t) = \vec{\mathbf{E}}_{0i}\exp\left[i\left(\vec{\mathbf{k}}_i\cdot\vec{\mathbf{r}}-\omega_i t\right)\right], \qquad \text{Equation 1.10}$$

where $\vec{\mathbf{E}}_{0i}$ is the amplitude vector (assumed constant in time), $\vec{\mathbf{k}}_i$ is the wave propagation vector, $\vec{\mathbf{r}}$ is the position vector (in Cartesian coordinates), ω_i is the temporal frequency of the wave, and t represents time. When this wave hits an interface at an incident angle θ_i between two different media, the reflected and transmitted wave can be expressed as

$$\vec{\mathbf{E}}_r(\vec{\mathbf{r}},t) = \vec{\mathbf{E}}_{0r}\exp\left[i\left(\vec{\mathbf{k}}_r\cdot\vec{\mathbf{r}}-\omega_r t+\varepsilon_r\right)\right], \qquad \text{Equation 1.11}$$

$$\vec{\mathbf{E}}_t(\vec{\mathbf{r}},t) = \vec{\mathbf{E}}_{0t}\exp\left[i\left(\vec{\mathbf{k}}_t\cdot\vec{r}-\omega_t t+\varepsilon_t\right)\right], \qquad \text{Equation 1.12}$$

respectively, where ε_r and ε_t are the phase constants relative to $\vec{\mathbf{E}}_i$, and for simplicity absorption is negligible. With further manipulation of these equations and by applying the laws of Electromagnetic Theory, two important laws are obtained:

$$\theta_i = \theta_r \text{ (Law of Reflection), and} \qquad \text{Equation 1.13}$$

$$n_i \sin\theta_i = n_t \sin\theta_t \text{ (Snell's Law of refraction),} \qquad \text{Equation 1.14}$$

where n is the index of refraction of each medium.

Since most of the time it is easier to measure power (or intensity) rather than the electric field of a wave, two dimensionless parameters are introduced to describe energy conservation across an interface. The first parameter is the reflectance R which is the ratio of the reflected power to the incident power:

$$R \equiv \frac{P_r}{P_i} = \frac{I_r A\cos\theta_r}{I_i A\cos\theta_i} = \frac{I_r}{I_i} \qquad \text{Equation 1.15}$$

where A is the surface area of interface. The second parameter is the transmittance T which is similarly defined as:

$$T \equiv \frac{P_t}{P_i} = \frac{I_t A\cos\theta_t}{I_i A\cos\theta_i} = \frac{I_t\cos\theta_t}{I_i\cos\theta_i}. \qquad \text{Equation 1.16}$$

Since we are assuming that there is no energy loss at either medium, the following relation is obtained from energy conservation:

$$R + T = \frac{P_r + P_t}{P_i} = 1. \qquad \text{Equation 1.17}$$

From Snell's Law, if $n_i > n_t$, there is a critical angle of incidence θ_c that will yield θ_t = 90°, T = 0, and R = 1. With this condition, the theory presented here implies that all the light is being reflected back into the first medium and none is being transmitted. This is the condition required to obtain total internal reflection. If the properties of the two media are known, then the critical angle is given by

$$\theta_c = \sin^{-1}\frac{n_t}{n_i}. \qquad \text{Equation 1.18}$$

Notice that the total internal condition can only be obtained if the light is propagating from an optically dense medium to a less dense medium. When the incident angle meets or exceeds the critical angle total internal reflection will occur and an evanescent wave is generated that propagates through the less dense medium.

Evanescent wave

Let the transmitted electric field be described by Equation 1.12, where

$$\vec{\mathbf{k}}_t \cdot \vec{\mathbf{r}} = k_{tx}x + k_{ty}y = (k_t \sin\theta_t)x + (k_t \cos\theta_t)y \qquad \text{Equation 1.19}$$

and since it is assumed a polarized wave, there is no z-component (z is in the direction perpendicular to the incident plane). Using Snell's Law and applying the TIR condition the following relations are obtained

$$k_{ty} = \pm ik_t\left(\frac{n_i^2 \sin^2\theta_i}{n_t^2} - 1\right)^{\frac{1}{2}} \equiv \pm i\beta\,, \qquad \text{Equation 1.20}$$

$$k_{tx} = \frac{n_i k_t}{n_t}\sin\theta_i\,. \qquad \text{Equation 1.21}$$

Combining these equations with Equation 1.12, the transmitted electric field is described by

$$\vec{\mathbf{E}}_t = \vec{\mathbf{E}}_{0t}\exp(-\beta y)\exp\left[i\left(\frac{k_t x n_i \sin\theta_i}{n_t} - \omega t\right)\right] \qquad \text{Equation 1.22}$$

Where, for convenience, the phase factor was dropped. This expression shows that the evanescent wave decays exponentially in the direction normal to the interface, towards the second medium with a decay constant length of β^{-1}. If glass (n_i~1.5) and water (n_t=1.33) are used as media, a scaling analysis for each of the terms for the decay constant gives

$$n_i \sim 1,\ n_t \sim 1,\ \sin\theta_i \sim 1 \therefore \left(\frac{n_i^2 \sin^2\theta_i}{n_t^2} - 1\right)^{\frac{1}{2}} \sim 1\,,$$

$$\beta = k_t\left(\frac{n_i^2 \sin^2\theta_i}{n_t^2} - 1\right)^{\frac{1}{2}} = \frac{2\pi n_t}{\lambda}\left(\frac{n_i^2 \sin^2\theta_i}{n_t^2} - 1\right)^{\frac{1}{2}} \sim \frac{2\pi}{\lambda}\,,$$

therefore, the evanescent wave becomes ~95% extinct at a distance ~$\lambda/2$. It is customary to excite at short wavelengths (488nm-514nm), resulting in an excitation thickness of about ~250nm. This thickness is small compared to the specimen height (~100μm), therefore only about 0.25% of the specimen height in solution is excited, eliminating most of the fluorescent background (Figure 1.3).

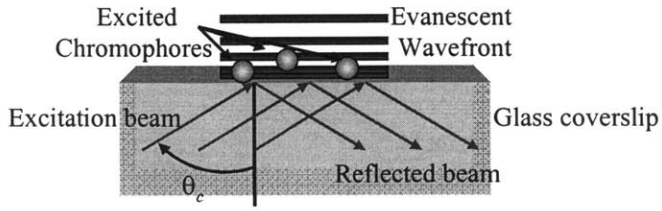

Figure 1.3. Schematic representation of TIRF.

An intriguing part of the evanescent wave is its energy source. If all the rays are being reflected back to the original medium, what is the energy source for the evanescent wave? For all the derivations presented here, an ideal infinite plane wave was considered, but in reality the optics and the laser source have finite size. This restriction gives rise to light diffraction which is not accounted for. Because of this phenomenon, some of the light will actually get transmitted to the second medium even at the TIR condition. This light "leakage" is the energy source of the evanescent wave.

Chapter 2: Experimental Equipment

For the proposed experiments, the equipment to be used consists of an optical trap combined with single molecule fluorescence microscopy capabilities. This equipment was designed and built around a commercially available microscope. The focus of this chapter is to present the design and construction of the experimental equipment.

2.1 Equipment Design, Construction and Capabilities

2.1.1 Design Objective

The objective of this work is to study how the binding kinetics between actin and actin binding proteins are affected by applying mechanical force to stretch an actin filament. The hypothesis behind these studies consists of a shift in the interaction energetics between two binding partners as application of force facilitates protein conformational changes. In order to perform these types of experiments, an instrument capable of both applying forces in the pico-Newton range and monitoring single molecule events is required. The design of this equipment is described below.

The objective of the design includes: (1) optical tweezers that can apply forces in the range of sub-pN to 100 pN; (2) position manipulation and detection in the nanometer range; and (3) single molecule fluorescence microscopy, with total internal reflection capabilities. All of these capabilities are integrated and automated by computer hardware and software (LabVIEW 6i; National Instruments Corp; Sunnyvale, CA), reducing human error during experiments. Automation of the system also provides high throughput of experimental runs, while recording real-time data at a fast rate (> 1 kHz). The key feature of the instrument is simultaneous combination of optical trapping and single molecule fluorescence microscopy.

2.1.2 Overview of Equipment

The instrument consists of a microscope, three different laser sources and two isolated boxes with multiple optical elements: one box houses the optical trap and position detection subsystem as well as the laser sources; and a second box encloses the single molecule fluorescence detection subsystem. The first box is on an elevated optical bread board that has been enclosed for eye protection, dust elimination and air currents

reduction. The box also has clear lids for regular inspection of the optics. The fluorescence detection dark box is completely sealed in order to prevent outside illumination from leaking in. All the equipment is mounted on an optical floating table that serves as a damper for structural vibrations. In the following sections, the construction and the components used in the design of the instrument will be discussed.

2.1.3 General Overview of Optical Path

A schematic with the optical design is shown in Figure 2.1. There are four light sources for the system: a bright field source as part of the microscope original design, and three laser sources, one for each of the functionalities of the instrument: position detection, trapping and fluorescent excitation. The optical path for each of the sources is described below.

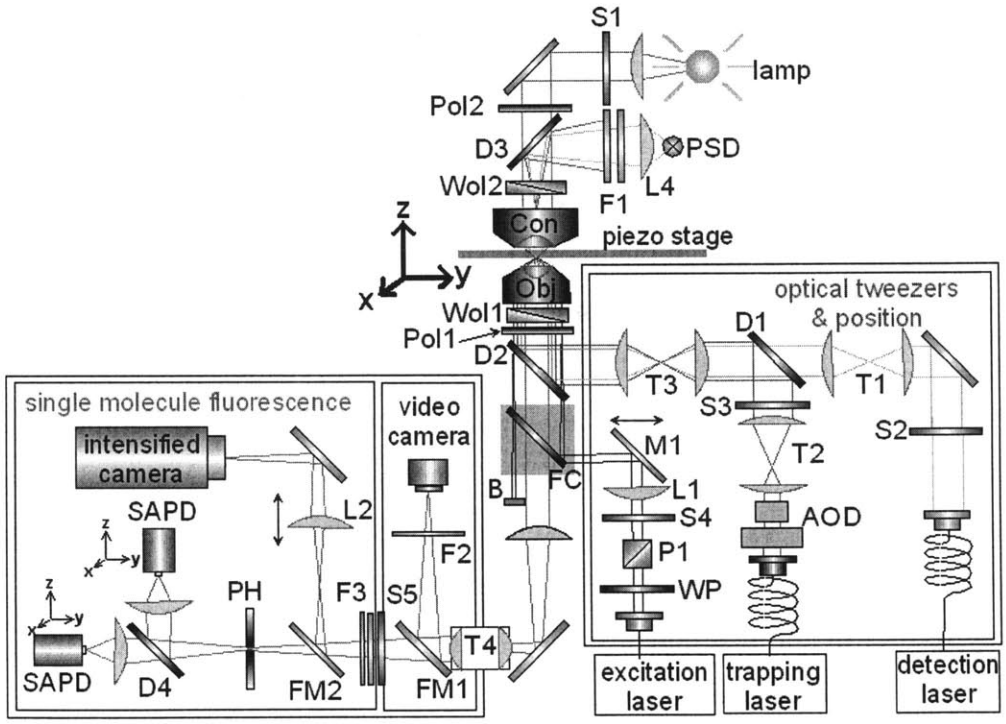

Figure 2.1. Schematic of instrument design. Adapted from Lang et al

Microscope and bright field illumination

The instrument is based on the TE2000-U inverted microscope (Nikon Instruments, Inc., Melville, NY) with a 100X 1.40NA Plan APO, oil immersion objective (Nikon Instruments, Inc.) (**Obj**; Figure 2.1). The high numerical aperture of the objective allows for both optical trapping and objective side total internal reflection microscopy. The microscope frame holds all the optics that combine the trapping laser, detection laser and

fluorescence excitation laser at the specimen plane. To control the location of the specimen a manual, 2-axis stage (75-MS; Rolyn Optics, Covina, CA) and a *xyz* piezo stage (P-517.3CD; Polytec PI, Tustin, CA) were mounted on the microscope after modifying the microscope original design (see section 2.1.4 below). The microscope frame was secured to the optical table by means of two adapter plates affixed to the base.

A 100W Hg arc lamp (Nikon Instruments, Inc.) is used as the bright field source. The amount of light that reaches the eyepiece is controlled by a set of polarizers (**Pol1**, **Pol2**; Figure 2.1). These in conjunction with a pair of Wollaston crystals (**Wol1**, **Wol2**; Figure 2.1) provide the phase contrast of the objects in the specimen plane. The light goes through the condenser (**Con**; Figure 2.1), the specimen slide and objective. Oil immersion objective and condenser are used. The image of the specimen plane is shuttled either to the eyepiece or a CCD video camera (CCD100; DAGE-MTI, Inc., Michigan City, IN) by means of a dial deflector inside the microscope. The CCD camera is connected to a monochromatic monitor (PVM-97; Sony Corporation of America, Parkridge, NJ), which sends the analog signal to a digitizer (Dazzle Digital Video Creator 150; Pinnacle Systems, Inc., Mountain View, CA) for capturing the image. The video-capture system described above works for both the bright field image and the fluorescence excitation image.

Position detection path

The source used for position detection is a near infrared fiber Bragg laser (980nm Optilock Pump; Corning Lasertron, Corning, NY; with LDC-3724B controller; ILX Ligthwave, Bozeman, MT) with up to 250 mW of power. For noise reduction, the laser power supply is located outside of the experimental room. The laser pump is coupled to an optical fiber and the output of the fiber is collimated using a beam collimator (F220FC-B; Thorlabs, Newton, NJ). The collimated beam is reflected through a pair of steering mirrors for alignment purposes (not shown in Figure 2.1). A 1:1 telescope (**T1**; Figure 2.1) is used to provide manual control over relative displacement between the detection laser and the trapping laser. The beam then goes through a dichroic (**D1**; Figure 2.1) that combines the detection beam with the trapping beam. After the dichroic, the beam passes through a second 1:1 telescope (**T3**; Figure 2.1) that provides coarse position manipulation and focusing of both the trapping laser and the detection laser

simultaneously. As the beam enters the microscope region, it is reflected along the optical axis by means of another dichroic (**D2**; Figure 2.1) coated for near infrared wavelengths. Once in the optical axis, the objective (**Obj**; Figure 2.1) focuses the beam on the specimen plane. The beam is re-collimated by the condenser (**Con**; Figure 2.1) and reflected by a second dichroic (**D3**; Figure 2.1) along the detection branch. This path includes filter (**F1**; Figure 2.1) that isolates the detection beam, and a lens (**L4**; Figure 2.1) that focuses the beam on the active area of a position sensing device (**PSD**; Figure 2.1). The PSD then transduces the intensity of the beam into *x-y* coordinates (see Position Detection section) represented by voltages, and this signal is monitored by a computer.

Trapping laser path

A near infrared laser (Compass 1064-4000M; Coherent, Inc., Santa Clara, CA) with a power output up to 4W is used to provide the trapping force. The laser source is located outside the experimental room (for noise reduction) and it is brought to the instrument by means of a single-mode, polarization maintaining optical fiber (PMJ-3S3S-980-6/125-3-30-1; OZ Optics, Carp, Ontario). An output coupler collimates the beam exciting the fiber. After being reflected by a pair of steering mirrors (not shown), the beam goes through a pair of acousto-optical deflectors (**AOD**; Figure 2.1) that provide fast and reproducible manipulation of the laser location on the specimen plane (see Position Manipulation Capabilities section). An iris is located right after the AOD's in order to block all the orders of the diffracted beam except the +1 order. The beam is then expanded by a 1:3 telescope (**T2**; Figure 2.1) in order to fill the back pupil of the objective to provide a larger intensity gradient, tighter focus and thus a larger trapping force. A dichroic mirror (**D1**; Figure 2.1) combines the trapping laser with the detection laser, and both go through the same path to the condenser. The objective focuses this beam in the specimen plane generating the trapping force. After the condenser, a set of filters (**F1**; Figure 2.1) block the trapping laser from getting into the PSD.

Fluorescence excitation laser path

A variable wavelength Argon ion laser (5425ASL-00; Ion Laser Technology, Inc., Salt Lake City, UT) provides the source for the fluorescence excitation. As with the

trapping laser, the laser source is located outside the experimental room and an optical fiber (QPMJ-33-488-3.5/125-3-30-1; OZ Optics) brings the beam into the room. The beam is sent to the microscope by a pair of steering mirrors. Then, the laser goes through a lens (**L1**; Figure 2.1, 15 cm focal length) that focuses the beam in the back focal plane of the objective. A movable mirror (**M1**; Figure 2.1) reflects the beam into the filter cube (**FC**; Figure 2.1) which sends the beam into the objective. The movable mirror facilitates the option of setting epifluorescence or total internal reflection (see Total Internal Reflection Fluorescence Microscopy section). When the system is set for TIRF the return beam is blocked by a hard obstruction (**B**; Figure 2.1) to prevent it from returning to the optical path.

As the excitation laser hits the specimen, fluorophores in solution get excited and emit light. This resulting emission is isolated by the filter cube which only passes the emission wavelengths. The fluorescence image is brought out of the microscope by a telescoping lens (**T4**; Figure 2.1) that enlarges the images 2.5 times. The beam enters a dark box with the single molecule fluorescence detection system (see Single Molecule Fluorescence Microscopy Capabilities section), and the image is collected by either the CCD camera or the photodetectors.

2.1.4 Microscope Modifications

Since several modifications had to be made to the microscope to implement the optical trapping capabilities, a computer rendered virtual model of the microscope frame (**1**; Figure 2.2**)** was created to facilitate component design. The objective turret, the filter cube spin wheel and the original specimen stage were removed in order to free more working space. The design also took the advantage of the infinity-capability of the objective by extending the optical path. A one-inch-thick aluminum base (**2**; Figure 2.2) was designed to hold all the components that align the laser beams with the optical axis. The base was designed such that it provides stability to the microscope and its attachment uses existing threaded holes on the microscope frame. In order to mount this base to the microscope frame, the illumination pillar was removed and the base was secured to the back of the microscope. A bracket (**3**; Figure 2.2) was designed to hold the base at the front of the microscope frame. Then, the illumination pillar was mounted on top of the base, raising the optical system by one inch from its original height. The rest of the

components were designed to compensate for this additional height. A pair of adapters (**4**, **5**; Figure 2.2) was made to hold both the objective and Wollaston prism, (**6**; Figure 2.2). These adapters were mounted onto the focusing platform of the microscope and replaced the objective turret. The design of these parts considered all the range of motion that the objective turret originally had plus additional clearance to avoid interference with other structural components.

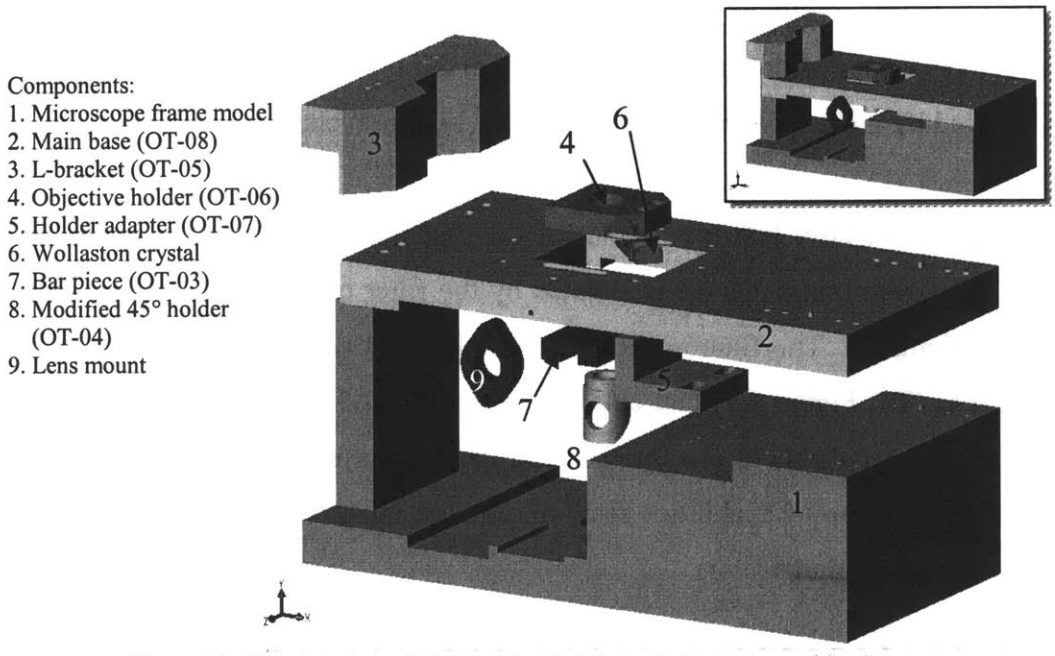

Figure 2.2. Microscope modifications (exploded view). *Inset*: Assembly view.

A dichroic mirror mounted on a modified 45° mirror mount (**8**; Figure 2.2) was used to reflect the incoming beam by 90° into the optical path. The 45°-mount was fixed to a bar piece (**7**; Figure 2.2) attached to the main base. This bar piece slides relative to the main base to align the incoming beam with the optical path. An additional threaded hole was made on the right side of the main base to hold one lens mount (**9**; Figure 2.2) from a telescope pair. Finally, a manual stage was mounted on top of the main base for coarse positioning of the specimen, and a nanometer-resolution piezo stage was placed on top of the manual stage for precise positioning (not shown in Figure 2.2).

In addition, changes to the condenser were necessary for implementing the position detection system (Figure 2.3). A hole to the right side of the condenser housing (**1**; Figure 2.3) was made in order to image the specimen plane outside the main optical path. A ring (**2**; Figure 2.3) that holds a dichroic was placed inside the condenser housing,

reflecting the image horizontally towards the detection branch (**4**; Figure 2.3). This branch holds all the optical components for the position detection capabilities of the instrument.

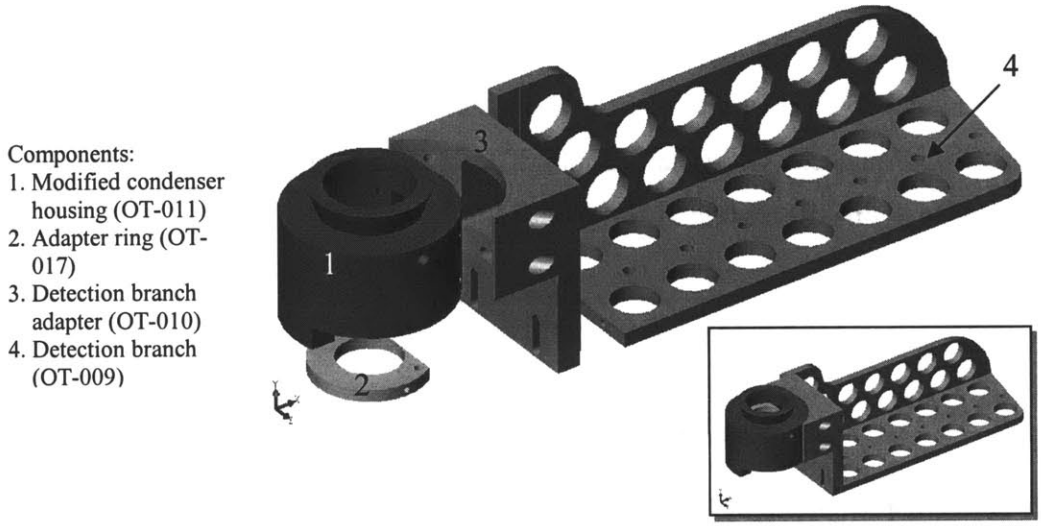

Figure 2.3. Condenser housing modification and detection branch (exploded view). *Inset*: assembly view

2.1.5 Position Detection Capabilities

The position detection system is based on the intensity profile generated by the scattering of a laser beam by a microsphere, and captured by a photodiode element. The element used in this instrument is a duo-lateral position sensing photodiode (DL100-7PCBA; Pacific Silicon Sensor, Inc., Westlake Village, CA) with an active area of 1 cm x 1 cm, and for simplicity it will be referred as position sensing device (PSD). This type of photodiode transforms an intensity profile input to an output with the location of the centroid of the intensity profile in terms of voltages in two axes (V_x and V_y) as well as the sum of voltages along both directions. The latter is used to normalize the former. The output signals are amplified and go through several filters to reduce external. An anti-alias filter (3384 Filter; Krohn-Hite Corp., Brockton, MA) set to one-half of the data collection further cleans the signal before being acquired by a 16-bit A/D board (PCI 6052E; National Instruments Corp; Austin TX). A calibration routine is then run to convert the output voltages into actual positions in the specimen plane (see section 3.1.1).

The PSD (Figure 2.1) is located at a conjugate optical plane of the condenser back focal plane in order to have the intensity profile independent of the focus location [38, 39]. For alignment purposes, the PSD is mounted on a three axis stage (MT-XYZ;

Newport, Irvine, CA). As the bead is displaced from the center of the detection beam waist, different scattering patterns are generated, and the photodiode converts these specific patterns into plane position of the bead. The mathematical derivation of the scattering profile of a laser beam through a microsphere is quite complicated, involving electromagnetic theory and optics design, and it is beyond the scope of this text. However, a model taken from literature will be compared to actual results to validate the instrument performance. Gittes and Schmidt [39] proposed a model to describe the intensity profile in one dimension as follows:

$$\frac{I_+ - I_-}{I_+ + I_-} \approx \frac{16}{\sqrt{\pi}} \frac{\kappa\alpha}{w_0^2} G(x/w_0), \qquad \text{Equation 2.1}$$

where

$$G(u) = \exp(-2u^2)\int_0^u \exp(y^2)dy, \qquad \text{Equation 2.2}$$

where x is the displacement of the center of the bead from the center of the trap. All the other parameters used are defined in Table 2.1.

Parameter	*Description*	*Definition*
λ_0	Wavelength of laser beam	978 nm
n_s	Index of refraction of solution	~1.33 for aqueous solution
n	Index of refraction of sphere	~1.45 for silica beads
a	Radius of the bead	0.5-1 μm
w_0	$1/e$ radius of focus of laser (Gaussian beam)	~ 0.53 μm
κ	Spatial frequency of laser	$2\pi n_s/\lambda_0 = 0.0085$ nm^{-1}
n_r	Relative index of refraction	$n/n_s = 1.053$
α	Uniform-field susceptibility	$a^3 \frac{n_r^2 - 1}{n_r^2 + 2} = 0.059a^3$

Table 2.1. Parameters used for position detection curve shape.

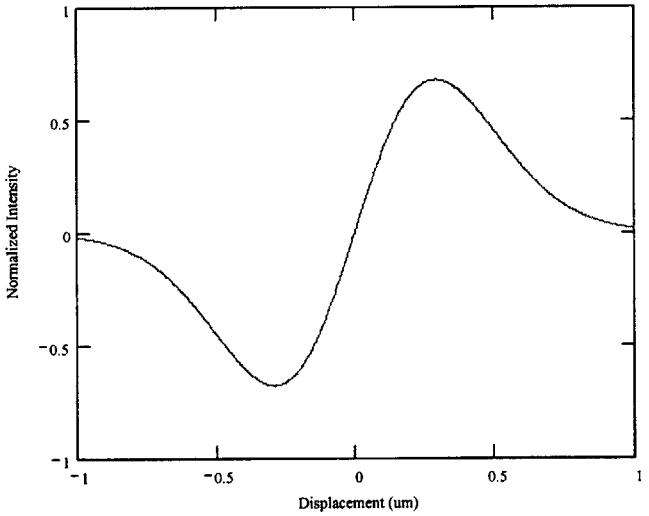

Figure 2.4. Model of expected intensity plot versus bead displacement from the center of the trap.

Figure 2.4 shows the normalized intensity (arbitrary units) as a function of the bead displacement from the center of the trap for a bead radius of 0.5μm and an estimated focus waste of 0.53μm. From the graph it can be noticed that for a given intensity there are two different values of displacement which introduce ambiguity to position detection. To avoid this ambiguity instead of using the entire displacement region, only 80% of the distance between the low and high peaks is used. Between these peaks, there is a unique displacement for a given intensity value, and the absolute position of the bead can be determined. The actual results of the position calibration for the designed system are shown in section 4.1.

2.1.6 Position Manipulation Capabilities

For fast manipulation of the trapping laser at the specimen plane, a pair of orthogonal acousto-optic deflectors (DTD-276HB6; IntraAction Corp., Bellwood, IL) is employed. The AOD's are driven by a frequency generator (DVE-4010C9; IntraAction) controlled by computer. The RF amplifier for these devices is placed outside the experimental room for noise reduction. One of the AOD's controls the x-displacement while the other controls the y-displacement. The two are placed close together at a plane that is conjugate to the back pupil of the objective, such that deflection of the beam at this plane produces translation of the beam at the specimen plane.

Inside the AOD's, a pressure wave at a certain frequency is transmitted to a crystal producing a density pattern. This pattern acts as a sinusoidal optical grating, diffracting the beam into its different orders. The angle at which each order occur relative to the zero order is given by

$$\theta_m = \frac{m\lambda_0 f}{v}, \qquad \text{Equation 2.3}$$

where m is the diffracted order (m = ...,-2,-1,0,1,2,...), λ_0 is the light wavelength, f is the acoustic wave frequency and v is the velocity of the sound wave across the crystal. Note that the zeroth order (m = 0) beam never changes its direction (θ_m = 0); therefore, it can not be used for position manipulation. Instead, the first order beam is used because it carries more power than the higher order diffractions, and the other orders are block by placing an iris right after the AOD's. Equation 2.3 shows that by controlling the acoustic frequency f, the angle of the first order beam can be changed, providing control of the laser trap focus at the specimen plane. By using two orthogonal oriented AOD's, control in two dimensions is obtained.

One drawback from the AOD's is that by using the first order diffraction, some of the incoming power is lost, and by using two AOD's in series the power gets further reduced. To compensate for this loss, the intensity of the incoming beam has to be increased, but this is also limited by the optics that are located before the AOD's, for example the optical fiber, such that they do not get damaged by excessive levels of power. Also the power efficiency can vary depending on the frequency; therefore, to obtain a stable trap, only a limited range of input frequencies should be used. In this case the frequencies used for both x and y deflections are typically between 25.5-26.5 MHz.

On the other hand, AOD's have a very fast response time, limited only by the ratio of the acoustic velocity and the diameter of the laser beam [38]. For the instrument set up, the fastest response is dictated by the computer speed, the software being used, and the communications ports.

2.1.7 Total Internal Reflection Fluorescence Microscopy Capabilities

In practice, there are two main configurations for implementing TIRF to a light microscope: prism method and objective lens method. The prism method uses a prism on top of the specimen slide and a laser beam is aimed at an angle equal or greater to the

critical angle. With this configuration, the evanescent wave is generated at the top of the slide and it travels down the specimen. Some disadvantages of this method are restricted access to manipulate the specimen, and imaging the evanescent wave through the bulk of the specimen. For these reasons and geometrical restrictions, the objective lens method was implemented in the instrument. With this technique the excitation beam is brought to a tight focus at the back focal plane of the objective in order to have a collimated output beam from the objective and satisfy the critical angle condition. The angle of incidence is controlled by adjusting the distance between the back focal point and the optical axis; that is, higher angles are achieved by greater offset distances. This behavior can be demonstrated by using geometrical optics, the paraxial approximation (small angles, i.e. $\sin\theta \approx \theta$) and the thin lens assumption. Consider the simple lens system in Figure 2.5, where a point source located at the back focal plane is imaged through the lens. The light propagation is described by the matrix

$$\begin{bmatrix} \theta_{out} \\ x_{out} \end{bmatrix} = \underbrace{\begin{bmatrix} 1 & -\frac{1}{f} \\ 0 & 1 \end{bmatrix}}_{\text{Lens matrix}} \underbrace{\begin{bmatrix} 1 & 0 \\ f & 1 \end{bmatrix}}_{\text{Light propagation from source to lens}} \begin{bmatrix} \theta_{in} \\ x_{in} \end{bmatrix} = \begin{bmatrix} 0 & \frac{-1}{f} \\ f & 1 \end{bmatrix} \begin{bmatrix} \theta_{in} \\ x_{in} \end{bmatrix}$$

where θ_{in} and θ_{out} are the input and output beam angles respectively, and x_{in} and x_{out} are the distance from the optical axis of the input and output beam respectively. Notice that if the point source is located at the back focal plane, the output angle is independent of the input angle and the former becomes

$$\theta_{out} = -\frac{x_{in}}{f} \qquad \text{Equation 2.4}$$

where the minus sign indicates that the output rays bend towards the optical axis. Therefore, by controlling the location of the input beam, the output angle (or the incident angle) is manipulated.

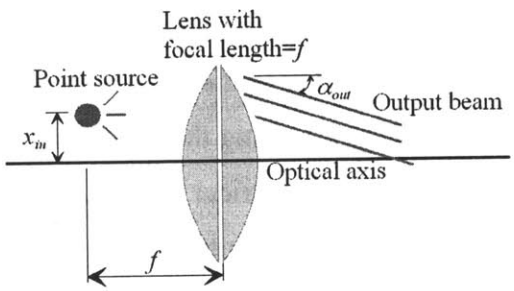

Figure 2.5. Optical system to demonstrate the realtions between point source location and output angle.

The system implemented to control the input location is depicted on Figure 2.6. A collimated beam enters the system and through a lens (**1**; Figure 2.6, and **L1**; Figure 2.1) that focuses the beam at the back focal plane of the objective. In order to maximize the excitation region, the focal length of the lens has to be as short as possible so that the back pupil of the objective is filled. Because of space limitations, the minimum focal length attainable was 12cm. To precisely focus the beam at the back focal plane of the objective, the lens is mounted on a 3-axes stage (**2**; Figure 2.6) with a range of 10mm in all three directions. The beam is then bounced from a mirror (**3**; Figure 2.6, and **M1**; Figure 2.1) mounted on a 1-axis stage (**4;** Figure 2.6), into a filter cube (**5**; Figure 2.6, and **FC**; Figure 2.1). The dichroic of the filter cube sends the excitation beam into the objective. The filter cube also serves as a filter, blocking the excitation beam from getting to the eyepiece and the imaging system. The angle of incidence at the specimen plane can be changed by moving the mirror stage (**4;** Figure 2.6) which offsets the focal point of the incoming beam from the optical axis. By moving the stage to either extreme, the TIR condition is obtained.

TIRF System:

1. Lens (KPX097 f=12cm, Newport) and lens holder (LMR1, Thorlabs)
2. 3-axes stage (M-MT-XYZ, Newport)
3. Reflective mirror (02 MPQ 007/023, Melles Griot)
4. 1-axis stage (MT-X, Newport)
5. Filter cube (Z488RDC or Z514RDC, Chroma)
6. Bottom plate adapter (OT-24)
7. Filter cube holders (M-MRL1.5, Newport)
8. Kinematic mount adapter (OT-25)
9. Kinematic mount (KMS/M and MH1, Thorlabs)
10. Magnetic mount (KB1X)
11. Magnetic mount adapter (OT-22)
12. Side adapter plate (OT-23)
13. Filter cube adapter plate (OT-26)
14. Input beam (from source)
15. Ouput beam (to objective)

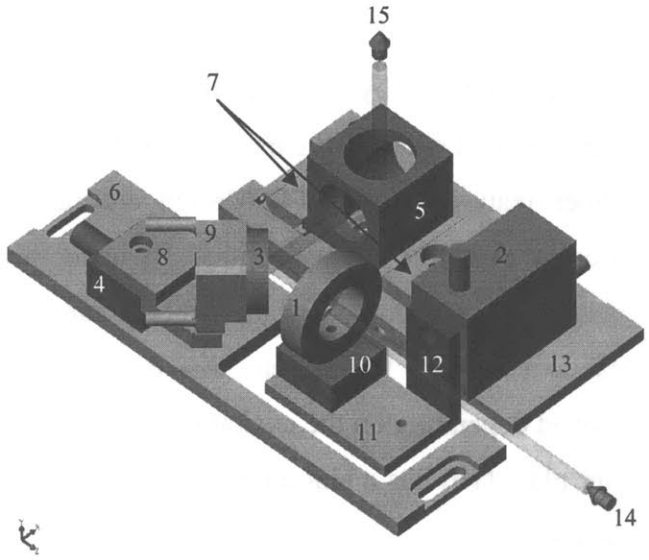

Figure 2.6. Schematic representation of TIRF system implemented in the Nikon TE2000-U microscope.

For many applications controlling the location of the input beam is not enough to obtain the TIR condition because the maximum angle of incidence achievable is strictly governed by the objective physical limitations. This limitation is the numerical aperture (*NA*) which is given by

$$NA = n \sin \theta \qquad \text{Equation 2.5}$$

where n is the index of refraction of the medium (usually oil, n=1.55) and θ is the half angle of the physical objective aperture from its focal point. Combining this equation with Snell's Law and the TIR condition a very important relationship is obtained:

$$NA = n_i \sin \theta_i = n_t . \qquad \text{Equation 2.6}$$

Equation 2.6 shows that in order to obtain total internal reflection, the numerical aperture must be equal or greater than the index of refraction of the specimen medium. For the instrument, an objective with numerical aperture of 1.40 was used, which is enough for most aqueous solutions applications which index of refraction range between 1.33 and 1.35.

Once the TIR condition is obtained, the return beam has to be blocked so it does not interfere with the image formed by the emission of the fluorescent dyes. To address this situation a small hard stop is placed on top of the filter cube (**B**; Figure 2.1).

The light source being used is an Argon ion laser with variable wavelength (488nm to 514 nm) and maximum power output of 10 mW. Since different applications require

different power inputs, an optical system to control the power input was placed right after the laser source. The system consists of a combination of a beam splitter and a $\lambda/2$ waveplate; therefore, by rotating the waveplate relative to the beam splitter, the amount of polarized light entering the microscope objective is precisely controlled.

Other features of the TIR design are its easy alignment, and its versatility of functioning at different wavelengths. By using the 3-axis stage, the 1-axis stage and the kinematic mirror mount, any input beam can be readily aligned with the microscope optical axis. Also, the system was designed such that filter cubes could be easily exchanged depending on the excitation wavelength to be used. In addition, the filter cube adapter plate (10) has a slot aligned with the optical axis for placing additional filters if necessary.

2.1.8 Single Molecule Fluorescence Microscopy Capabilities

The system for single molecule fluorescence microscopy is depicted in lower left side of Figure 2.1. Once the image of the fluorescence emission enters the "dark box", it can either be sent to a CCD video camera or the single molecule detection system by changing the setting of an electronic flipper mirror (**FM1**; Figure 2.1). To avoid excessive intensity from reaching the silicon avalanche photodiodes (**SAPD**; Figure 2.1) or the intensified camera, a shutter (**S5**; Figure 2.1) and a set of filters (**F3**; Figure 2.1) are placed at the entrance of the single molecule detection system. A second flipper mirror (**FM2**; Figure 2.1) is used to send the image to either the intensified camera or the SAPD's. Because very low light intensity is required, the intensified camera provides a way of actual visualization of the image, that otherwise with the regular CCD camera it could not be seen. A lens (**L2**; Figure 2.1) relays the image to the active area of the intensified camera. For the actual single molecule detection, the flipper mirror FM2 is lowered so that the image is directed towards the SAPD's. Before reaching the SAPD's, the beam goes through a pinhole (**PH**; Figure 2.1) which is located at a conjugate image plane. The purpose of the pinhole is to limit the size of the beam getting to the SAPD in such way that they only collect light from a very limited region, preventing them from getting saturated. The pinhole has a diameter of 300 μm which gets transferred to a size of 1.5 μm at the specimen plane. By limiting the size of the beam, the effective excitation zone at the specimen plane is given by a volume enclosed by the surface area

of the pinhole, and the height of the evanescent wave. This is described as an imaginary cylinder at the specimen plane with an approximate volume of 0.5×10^{-15} L (or 0.5 fL) (see Equation 4.1 below). After the pinhole, the image reaches the photodiodes, which provide an electronic output depending on the amount of intensity that reaches the active area. The output is collected by a computer, which generates a strip-chart of the intensity as a function of time. By using this method, particular events can be tracked and the duration of such event can be precisely determined.

As described in this chapter, the experimental design has capabilities for optical trapping, position detection and single molecule fluorescence, all in one instrument. However, the precision, accuracy and resolution have not been mentioned yet. To obtain these properties from the equipment, it is necessary to run multiple calibrations, which are mostly automated in order to reduce human error and external noise. These calibrations are described in detail in the following chapter.

Chapter 3: Experimental Methods

In this chapter, the methods used to calibrate the instrument as well as to prepare the biological assay are presented.

3.1 Equipment Calibration

In order to interpret the data collected during experiments, calibration is required for the position and force measurements. The following sections describe the calibration procedures for the system.

3.1.1 Position Calibration Method

To determine the force exerted on a particle by the trap, the exact position of the particle relative to the center of the trap must be known. Therefore, it is first necessary to calibrate the PSD voltage output and the AOD frequencies with a known position reference: the piezo stage.

Calibration of the AOD's is performed in two steps. First, a flow cell with silica beads (1μm diameter) stuck to the coverslip surface is placed on the microscope. The image acquired by a CCD camera and an arbitrary bead is selected as the calibration reference. Using the mechanical stage, the specimen is moved such that the bead is in one corner of the field of view of the camera. The piezo stage is set to move in a 2-dimensional grid pattern in discrete steps of 1μm while resting in each position for several seconds. A still image from the CCD camera is recorded at each location. The images are then analyzed using WinSpec32 (Roper Scientific, Inc., Trenton, NJ) to locate the centroid of the bead in terms of pixel coordinates at every time point. Then, the pixel location is correlated linearly to the position of the piezo stage in both x- and y-directions.

The next step consists of a loading another slide with free beads that can be trapped in solution. The bead is moved in a 2-dimensional grid pattern by changing the input frequencies of the AOD's in steps of 500 kHz, and still images are recorded at each step. The images are analyzed locating the centroid of the bead, and a linear correlation between the input frequency and pixel displacement is obtained. Combining the position-to-pixel and pixel-to-AOD frequency, a linear relationship between displacement and input frequency in the form of

$$\Delta x = A_x \Delta Hz_x \qquad \text{Equation 3.1}$$

is obtained, where A_x is the conversion factor (along the x-axis) with units of distance per unit frequency. This calibration procedure yielded a conversion factor of 1148 nm/MHz in the x-direction and 1041 nm/MHz in the y-direction.

With the AOD's calibrated, a relationship between PSD voltage output and AOD frequency input can be found. A bead is trapped and moved in a grid pattern using the AOD's, while the PSD collects the overall scatter from each location and converts to an x-y voltage. A 2-D surface is obtained for both the voltages output of the PSD as shown in Figure 4.1. To avoid ambiguity (see Position Detection Capabilities section above), a region consisting of 80% percent of the peak-to-peak distance is selected as the detection zone. A 2-D, fifth order polynomials is fitted to convert the PSD output into AOD's frequency in the form of

$$MHz_x(V_x, V_y) = C_0 + C_1 V_x + C_2 V_y + \ldots + C_{20} V_x^{\,3} V_y^{\,2} + C_{21} V_x^{\,2} V_y^{\,3}, \qquad \text{Equation 3.2}$$

$$MHz_y(V_x, V_y) = D_0 + D_1 V_x + D_2 V_y + \ldots + D_{20} V_x^{\,3} V_y^{\,2} + D_{21} V_x^{\,2} V_y^{\,3} \qquad \text{Equation 3.3}$$

where V_x and V_y are the output voltages of the PSD, and C_i and D_i are the fitted coefficients of the polynomials. With these results, and Equation 3.1, output voltages from the PSD can be converted in 2-D position.

3.1.2 Force Calibration Methods

In general, the energy used to trap particles can be modeled as a harmonic potential well, similar to a linear elastic (Hookean) spring, where the energy stored in the spring system is given by

$$U_{spring} = \frac{1}{2}\alpha \Delta x^2. \qquad \text{Equation 3.4}$$

where Δx is the distance from the center of the particle being trapped to the center of the trap, and α is the trap stiffness in units of force per unit length. This assumption simplifies the force computation but it is only valid for small displacements from the center of the trap, usually around 100 nm. Using the spring model, the force exerted by a laser trap on a particle can be described as a linear relationship with the displacement Δx,

$$F_{trap} = \alpha \Delta x. \qquad \text{Equation 3.5}$$

There are different approaches for determining the trap stiffness using either fluid mechanics or statistical mechanics. Here, one fluid mechanics method (Stoke's drag) and

two statistical mechanics methods (Equipartition Theorem and frequency response) are discussed.

Stoke's drag method

The Stoke's method uses an imposed flow velocity to apply a viscous drag force to the trapped bead (Equation 3.1). The drag force generated by viscous flow is described as

$$F_{drag} = \gamma \dot{x}. \qquad \text{Equation 3.6}$$

where γ is the drag coefficient ($\gamma = 6\pi\mu a$, a is the bead radius, μ is the fluid viscosity) of the particle (in this case, a bead), and $\dot{x}$ is the relative velocity between the particle and the fluid. Assuming that the only forces involved are the viscous drag and the trapping force and they are balanced, the trap stiffness can be computed by combining Equation 3.5 with Equation 3.6 and expressing the drag coefficient in explicit form:

$$\alpha = \frac{6\pi\mu a\dot{x}}{\Delta x}. \qquad \text{Equation 3.7}$$

From Equation 3.7, there is a linear relationship between displacement and fluid velocity, with a slope of the ratio of the drag coefficient to the trap stiffness. To obtain the data, the piezo stage is moved in one direction at incremental velocities while the displacement of the bead is simultaneously monitored. The data are then analyzed and fitted to Equation 3.7 to obtain the trap stiffness. Notice that the trap stiffness is also proportional to the bead size and fluid viscosity; therefore, if a stronger or weaker trap is required, this parameter can be changed to fit the desired application. It is also important to note that the Stoke's method generates relatively large bead displacements compared to other methods (Equipartition, power spectrum, etc.); therefore, it probes the outer edges of the trap potential well. The following paragraphs describe two methods of probing the stiffness near the center (small displacement) of the trap.

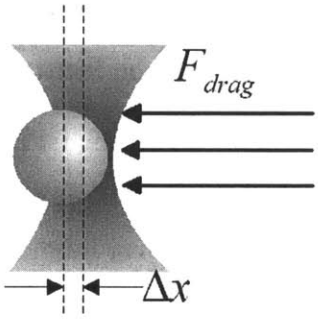

Figure 3.1. Stoke's force calibration method.

Equipartition method

The Equipartition Theorem proposes that if the energy of a molecule depends on the square of a parameter, then the mean energy associated with each degree of freedom

measured by that parameter is ½ k_BT. If the trap is modeled as a Hookean spring, then the Equipartition Theorem (in one dimension) implies the following:

$$\frac{1}{2}k_BT = \frac{1}{2}\alpha\langle x^2\rangle. \qquad \text{Equation 3.8}$$

where $\langle x^2\rangle$ is the variance of the position of a trapped bead.

To run this calibration, a bead is trapped and the position of the bead is recorded, where the user defines the scan rate and number of data points. From these data, the variance of the position relative to the center of the trap is computed and the trap stiffness is obtained using Equation 3.8. This method requires detailed knowledge of position calibration.

Power spectrum method

The dynamics of a trapped bead in a harmonic potential well surrounded by a fluid is described by the Langevin equation

$$m\ddot{x}(t) + \gamma\dot{x}(t) + \alpha x(t) = F(t) \qquad \text{Equation 3.9}$$

where m is the mass of the particle, $F(t)$ is the thermal force (or Langevin force) [38], and the other parameters have been defined above. Thermal force for a particle in Brownian motion is given by [40]

$$F(t) = (2k_BT\gamma)^{1/2}\eta(t), \qquad \text{Equation 3.10}$$

where k_BT is the thermal energy of the particle, and $\eta(t)$ represents the random Gaussian process component of the Brownian motion. The first term of Equation 3.10, $m\ddot{x}(t)$, represents the inertial effect, the term $\gamma\dot{x}(t)$ represents the dissipation (or viscous) effect, and $\alpha x(t)$ is the trapping force. For most biological and optical trapping applications, the system is at a low Reynolds number regime [40]. In this regime, viscous effects dominate over inertial effects, and the latter are considered negligible. This simplifies the Langevin equation to

$$\gamma\dot{x}(t) + \alpha x(t) = (2k_BT\gamma)^{1/2}\eta(t). \qquad \text{Equation 3.11}$$

Since the power spectrum is based on the frequency response of the system, Equation 3.11 is converted to the frequency domain by means of the Fourier Transform with respect to t. After some manipulation, it can be shown that the frequency response fits a Lorentzian described by

$$X(f)X^*(f) = \frac{k_B T}{2\pi^3 \gamma\left(f^2 + f_c^2\right)} \qquad \text{Equation 3.12}$$

where $X(f)$ and $X^*(f)$ are the Fourier transform and the complex conjugate of the Fourier transform of $x(t)$ respectively, f is the frequency of data acquisition and f_c is the roll-off frequency which is given by

$$f_c = \frac{\alpha}{2\pi\gamma}. \qquad \text{Equation 3.13}$$

To perform this calibration, the same data from the Equipartition Method are used. The data are Fourier transformed and the power spectrum is obtained. The data are fit to Equation 3.12, and a value for the roll-off frequency is determined. Then, Equation 3.13 is used to solve for the trap stiffness α.

After all the force calibrations are completed, they are compared with each other. Typically, if the instrument is set-up correctly and all the optics are aligned, the stiffness from the three methods are within a factor of 2 or less between each other. The results of these calibrations are presented in section 4.1

3.2 Biological Assay Preparation

The proposed experimental assay *in vitro* is depicted in Figure 3.2. An actin filament is anchored to a coverslip by coating the surface with a ligand, in this case myosin. The free end of the filament is attached to a myosin-coated microsphere which provides the handle to apply the tensile forces using the optical trap. Using the manual and piezo stages, the assay is positioned such that the bead and the surface attachment are outside of the fluorescence collection zone. This fluorescence collection zone consists of a "cylinder" with boundaries given by the height of the TIRF evanescent wave and the diameter of the

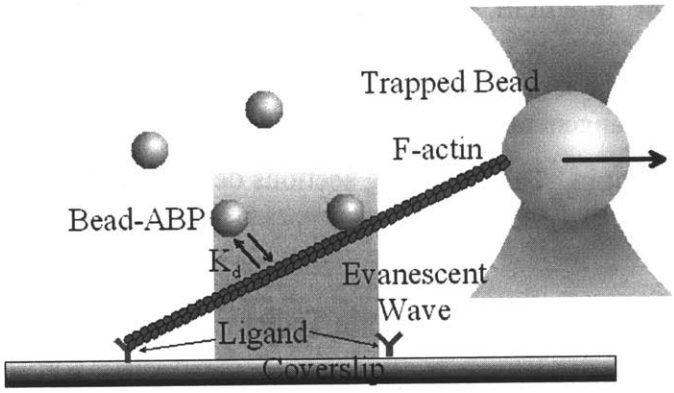

Figure 3.2. Experimental assay. Actin filaments are held fixed on the surface by coating a cover glass with ligand (see text). The other end of the filament is bound to a bead which is trapped. Binding between actin filaments and fluorescently labeled ABP's are monitored in the region of the evanescent wave.

pinhole image as described above (section 2.1.7). This allows for the combination of optical trapping with single molecule microscopy, since the trapping and detection beam are outside the fluorescence collection zone; therefore, the detectors will not capture their emission.

Once the actin filament is placed in the excitation zone (as shown in Figure 3.2), a steady force is applied to the filament by moving the piezo stage relative to the trapped bead. Then, a solution containing an actin binding protein is introduced to the experimental flow channel. The ABP will either be labeled with a fluorescent antibody, or bound to a small fluorescent bead. The concentration of the ABP used is such that, on average, there is only one molecule (or one bead) in the fluorescence collection volume. The time spent by a molecule or bead in the excitation zone is recorded by the photodiode (**SAPD**; Figure 2.1) and its duration depends on whether the protein is bound to the filament (binding event) or not (diffusion of bead across the excitation zone). The data are analyzed (see section 4.3.3 for details) and a fit value of the dissociation rate is obtained (k_{off}). The experiment is repeated applying different forces to obtain a relationship between filament tension force vs. k_{off}.

In previous work [41-43], actin was anchored to a nitrocellulose surface using myosin or α-actinin as surface linkers, and beads were coated with myosin, gelsolin or streptavidin (with biotinylated filament). Here, a combination of myosin-actin-myosin arrangement is presented, and the initial actin binding protein to be tested will be α-actinin. The following sections describe the protocols to construct these configurations *in vitro*.

3.2.1 Building an F-actin Tether

Actin polymerization

Globular actin (G-actin) from rabbit skeletal muscle (AKL-99, >99% pure; Cytoskeleton, Inc., Denver, CO) was polymerized and labeled with Alexa-Fluor 488 phalloidin (A-12379; Molecular Probes, Eugene, OR) as follows: actin monomers were diluted in G-buffer (5 mM Tris-HCl [pH 8.0], 0.2 mM $CaCl_2$, 0.5 mM DTT and 0.2 mM ATP) to a final concentration of 0.5 mg/mL, and were left on ice for one hour. Then, 2 μL of 6 μM Alexa-Fluor 488 phalloidin (diluted in ethanol) was added to an empty 0.5

μL vial and let to dry for one hour at room temperature in dark. A volume of 100 μL of diluted actin was added to the phalloidin vial, and 10 μL of F-buffer (50 mM Tris-HCl [pH 8.0], 20 mM $MgCl_2$, 1 M KCl, 2 mM $CaCl_2$, 5 mM ATP, 2 mM DTT) were added to initiated the polymerization process. This actin solution was left on ice for one hour in order to reach steady state, where the filaments grew to an average length of ~10 μm. The actin filaments remained functional for at least one week. To observe the actin filaments using fluorescence microscopy, the actin solution was diluted 1:100 in F-buffer, to a final concentration of ~ 5 μg/mL (see Figure 4.8).

Fluorescently labeled myosin coated beads

Beads coated with myosin were prepared per Dupois *et al* [41] with some modifications. Polystyrene beads of 1 μm in diameter (Polybead Amino Microspheres; Polysciences, Warrington, PA) were diluted to a final concentration of ~ 4 x 10^8 microspheres/mL in Myosin buffer (300 mM KCl, 5 mM $MgCl_2$, 25 mM imidazole, 1 mM EGTA and 10 mM DTT, pH 7.4). A volume of 1 mL of bead solution was sonicated for 2 minutes at 40% using a cup sonicator (Vibracell; Sonics & Materials, Inc., Newtown, CT). Then, 200 μL of 2.0 mg/mL of monomeric myosin from rabbit skeletal muscle (MY02; Cytoskeleton, Inc.) was mixed with 200 μL of microsphere solution to a final concentration of 1.0 mg/mL of myosin and ~ 2 x 10^8 microspheres/mL. The solution was incubated for 5 minutes at room temperature. Excess myosin was removed by centrifugation for 5 minutes at 10,000 rpm. The myosin-bead pellet was resuspended with 400 μL of 50 μg/mL of Alexa Fluor 488-BSA (A13100; Molecular Probes, Inc.) in Myosin buffer and sonicated for 20 seconds at 30%. The solution was incubated for 2 minutes at room temperature. Excess dye was removed by centrifugation for 5 minutes for 10,000 rpm, and resuspended with 400 μL of Assay buffer (25 mM KCl, 5 mM $MgCl_2$, 25 mM imidazole, 1 mM EGTA and 10 mM DTT, pH 7.4). After sonication for 20 seconds at 30%, the solution was washed twice and resuspended each time in Assay buffer, sonicating for 20 seconds at 30% after every resuspension. The beads were stored in dark at 4°C and were functional for at least one week.

Binding F-actin to myosin coated beads

A volume of 3 μL of 5 μg/mL of labeled F-actin was mixed with 345 μL of myosin coated beads. The final concentrations are ~ 40 ng/mL F-actin and ~ 5 x 10^7 beads/mL. The solution was incubated for 10 minutes at room temperature, and stored at 0°C prior use.

Preparation of flow channel

Coverslips (22 x 40 mm No. 1 ½; Corning, Inc., Corning, NY) were cleaned and etched with 1.0 M KOH dissolved in ethanol (200 proof). A flow channel was made by placing two strips of double-sided tape (~ 100 μm thick) at about 4 mm apart on a microscope slide, and placing an etched coverslip at 90° from the long edge of the slide. The total volume of the flow channel is ~ 10 μL. The insertion of aqueous solution into the flow channel was by means of capillary effect.

Preparation of actin tethers

A volume of 10 μL of 0.03 mg/mL of monomeric myosin in Myosin buffer was forced into the flow channel, followed by an immediate addition of 16 μL of 0.5 mg/mL of bovine albumin serum (BSA) in Assay buffer. This step removes any unbound myosin from the flow channel as well as blocks the rest of the coverslip surface. Then, 16 μL of F-actin/myosin bead solution was introduced to the flow channel.

The system was placed in the microscope and observed using fluorescence microscopy. Two approaches were used to find the surface-actin-bead tether: 1) scan the surface until a tether is found, or 2) actively construct the assay by trapping a bead and rubbing it against the free end of an actin filament with one end bound to the surface.

3.2.2 Introducing Actin Binding Proteins

As of the time this document was prepared, α-actinin was not prepared for the experimental assay. Here it is described how ABP's will be prepared and introduced to the experimental assay for future experiments.

Labeling α-actinin

There are two approaches for labeling α-actinin: (1) fluorescent antibody, or (2) fluorescent microbead. Using a fluorescent antibody has the advantage of providing a

small tag to the protein, with minimal effects on its diffusion, but on the other hand, photobleaching effects become evident. To avoid photobleaching, a dye has to be selected with a lifetime that is much longer than the experimental duration time. Finding the right dye could become tedious work, having to run several trial-and-error experiments to determine the right combination between excitation power and photobleaching effects.

With the second option, binding α-actinin to a bead increases the diffusion timescale since beads are usually much larger than the actual protein, so selection of bead size has to be carefully considered (see section 4.3.2). Also, to link the protein to the bead may require an additional tether, for example, α-actinin to mouse antibody, to bead coated with goat-anti-mouse. This kind of tether might require time to be developed. Conversely, using beads eliminates the photobleaching effects and a stronger signal is produced. An alternative of beads are quantum dots. These particles range between 1 nm to 10 nm in diameter, and are commercially available functionalized with different antibodies and fluorescent colors. Quantum dots are becoming commonly used for experiments of this kind as well as labeling molecules inside the cell for particle tracking experiments. The availability and use for quantum dots will be further investigated.

For future applications, preliminary experiments will be tried using these options and the optimal (photobleaching, diffusion, easiness of preparation, fluorescent signal, etc.) system will be selected.

Introducing labeled α-actinin

Once a procedure of labeling α-actinin is selected, the protein has to be introduced to the experimental assay. The concentration to be used is 3.75nM for protein labeled with antibody or 2.26×10^{12} beads/mL when using beads or quantum dots (see section 4.3.1). Once the actin tether is placed on the excitation zone, the solution containing the labeled α-actinin is flowed into the channel, and the duration of binding events are monitored by the photodiode. The data collected is then analyzed and the dissociation rate is determined (see section 4.3 for details). The specifics of introducing labeled α-actinin have to be worked out by experimental trials.

In this chapter, the instrument calibration procedures and actin tethers methods have been described. In addition, it was presented two different methods to attempt the labeling α-actinin for future experiments. Once the actin tether and the labeled protein are completely resolved and combined, experiments can be performed to reach the final goal of this research: determine force-dependent binding kinetics between actin and actin binding proteins, in this case α-actinin.

Chapter 4: Results

Here, the results of the instrument design as well as the actin tether are presented.

4.1 Instrument Design Results

Several different results for the instrument design are presented: position detection resolution, trap stiffness and beam profile, TIRF, and single molecule detection.

4.1.1 Position Detection and Manipulation

After implementing the position detection system, the PSD was tested and the voltage response representing the intensity of scatter is shown in the plots of Figure 4.1 for both x-axis and y-axis. This was done by scanning the AOD's in a grid pattern, moving the trap beam relative to the detection beam, and collecting the scatter signal on the PSD. Note in these surface plots, if a vertical cross section is taken, the resulting curve follows the same shape as the model prediction (Figure 2.4). Also, the x and y axes represent the grid position corresponding to location of trap in specimen plane. By combining the output between the x and y axes, the limit of the detection region (80% of peak-to-peak distance) is defined, where anything laying outside that region will result in ambiguous location making the data invalid. After calibration, the detection region is enclosed by a circle whose diameter is approximately 231 nm (Figure 4.2).

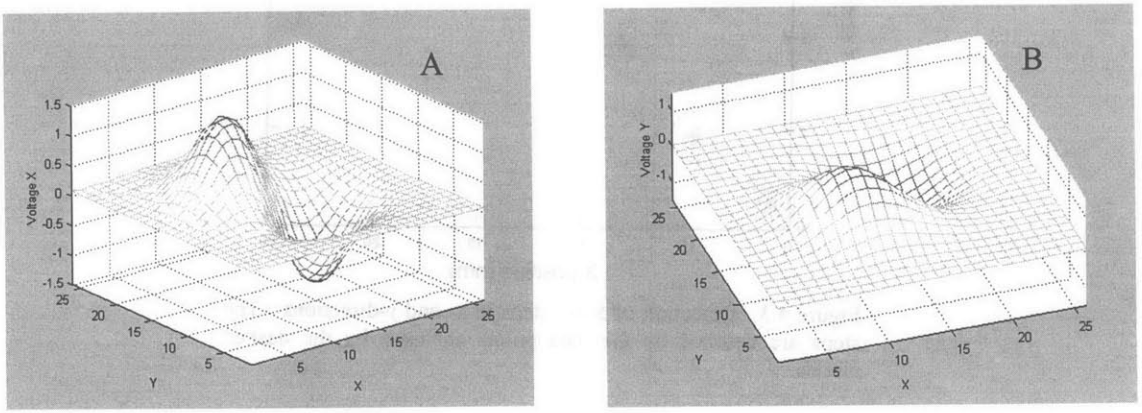

Figure 4.1. Intensity profile generated by a displacement of a bead from the center of the detection laser focus. A, surface plot for x-axis. B, surface plot for y-axis. Note that A and B are 90° apart from each other.

To test the threshold of the position detection, a bead stuck to the surface was moved in decreasing step-size until the signal from the PSD could not be distinguished without ambiguity. The smallest step size that the PSD can currently detect is approximately 5 nm (Figure 4.3).

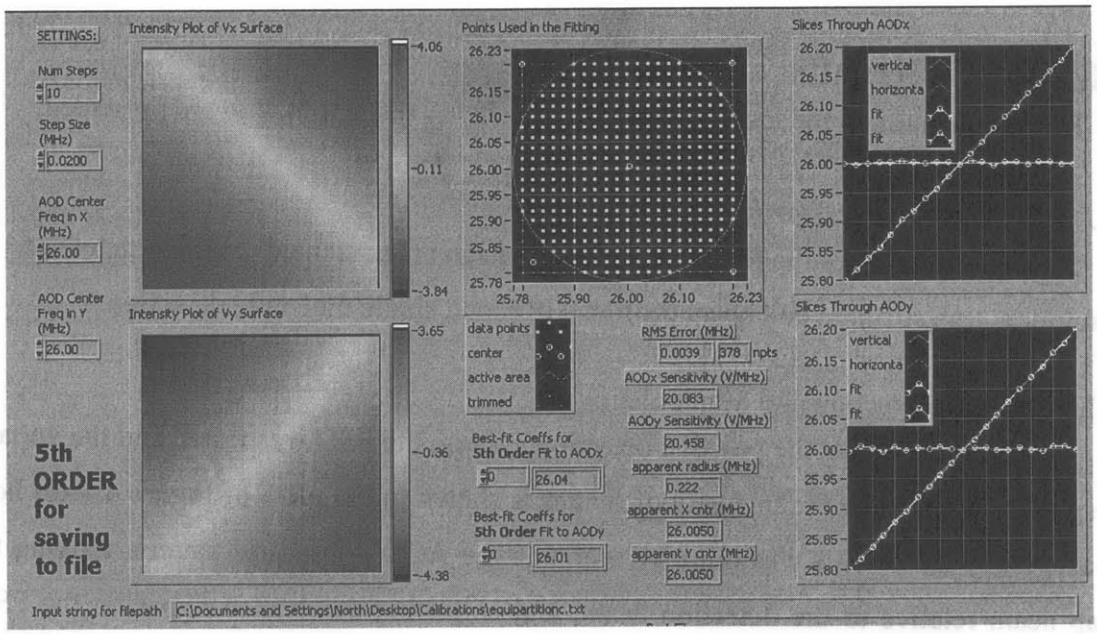

Figure 4.2. PSD calibration using AOD scanning. The PSD voltage and AOD frequency are fitted to a fifth order polynomial. The detection zone is determined by a circular surface with a radius of 0.222 MHz (231 nm).

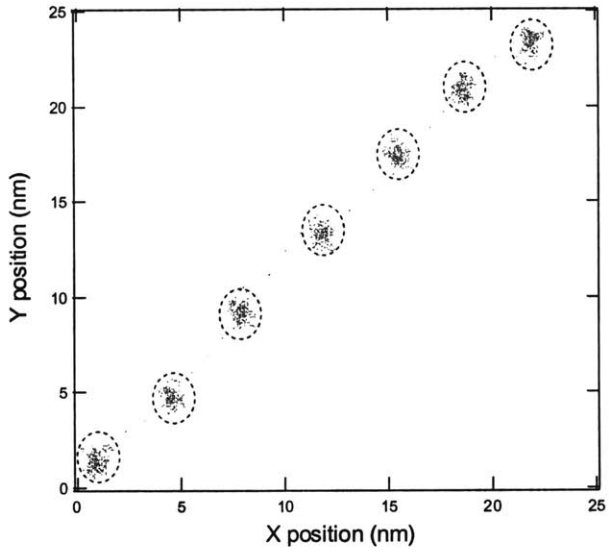

Figure 4.3. Detection of 5 nm steps in x- and y-directions. The steps are denoted by the data points enclosed by the dashed circles.

4.1.2 Trap Stiffness and Profile

The data for the Stoke's drag calibration method is shown in Figure 4.4, for a 0.5 μm bead and a fluid velocity of 0.15 μm/sec. The position of a trapped bead is monitored for forward and reverse flow in both x- and y-axis. Using both Equation 3.7 and the average bead displacement, the stiffness is computed for both axes. For this calibration, the

computed trap stiffness are α_x = 0.052 pN/nm and α_y = 0.066 pN/nm in the x- and y-directions respectively.

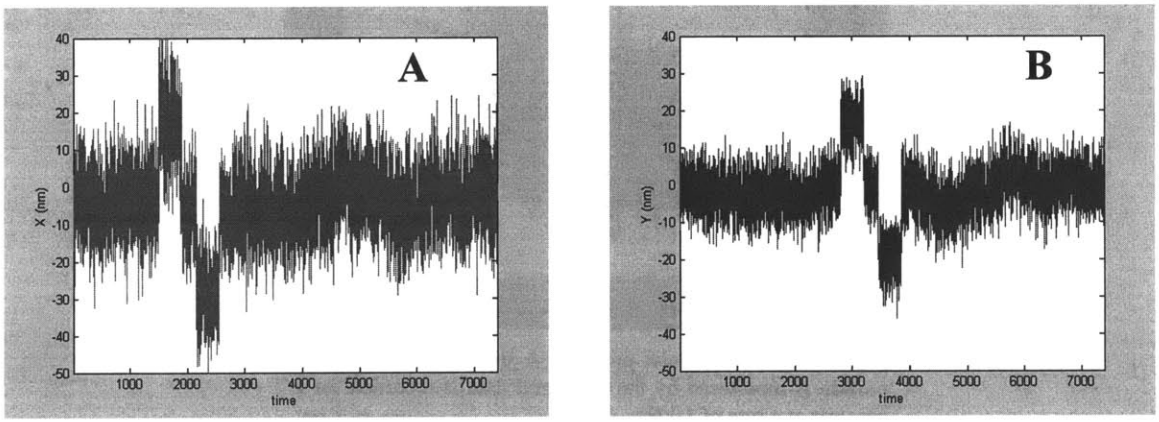

Figure 4.4. Drag force calibration method. A flow with a velocity of 0.15 μm/sec is applied in the forward and reverse direction along both x and y coordinates. A, calibration for x-axis resulted in a stiffness of 0.052 pN/nm; *B*, calibration for y-axis resulted in a stiffness of 0.066 pN/nm. Data recorded at a rate of 1-kHz.

Two additional methods for stiffness calibration rely on statistical mechanics approaches: Equipartition and power spectrum. The data collected for these approaches are shown in Figure 4.5. Data were collected at 1 kHz for 2.7 seconds for a total number of 2,700 data points. Figure 4.5 also shows that the waist profile of the trap at the specimen plane is elliptical, with its major axis tilted from the x-axis. This could be the result of beam misalignment, optical aberrations along the optical path, or light polarization. This topic is discussed in greater detail on chapter 6. Under optimal conditions, the trap profile should be in a circular shape centralized at the origin; however, it will always be elliptical with a polarized input beam.

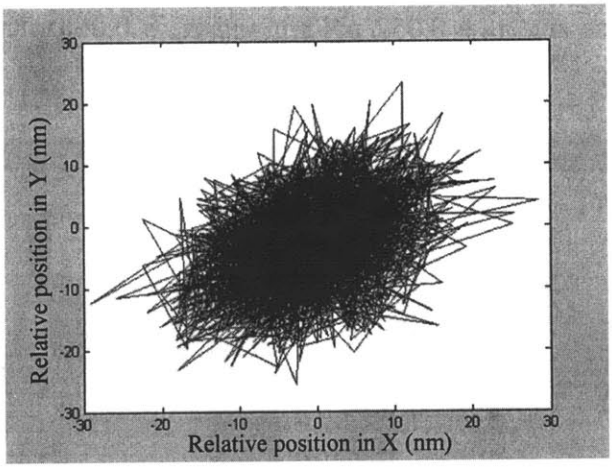

Figure 4.5. Trap waist profile. A trapped bead Brownian motion is monitored by the PSD, and data is recorded for 2.7 seconds at a rate of 1-kHz.

Because of the asymmetric trap, the trap stiffness between the Stoke's method and Equipartition method can not be directly compared, since the axes of the Stoke's method are rotated 45° relative to the axes of the Equipartition method. The data in Figure 4.5 are shown in Figure 4.6 with the axes rotated to match with the Stoke's method. Computing the variance along these new coordinates and using Equation 3.8, the results are $\alpha_x = 0.059$ pN/nm and $\alpha_y = 0.131$ pN/nm. These results show the non-symmetry of the trap stiffness, where the trap is much weaker on the x-axis, giving rise to an elongated shape in that direction. Comparing these results with Stoke's drag method the trap stiffness in the x-axis agree within a factor of 1.1 (Equipartition/Stoke's). On the y-axis the stiffness ratio of Equipartition to Stokes is ~2. These results demonstrate good agreement between the fluid mechanics approach and the statistical mechanics approach, but closer results can be obtained by optimizing the trap.

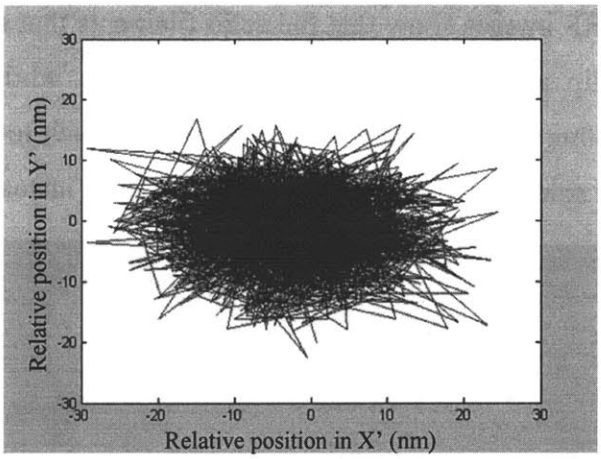

Figure 4.6. Trap profile with axes rotated 45°.

The results of the power spectrum method are shown in Figure 4.7. The computed trap stiffness is $\alpha_x = 0.060$ pN/nm and $\alpha_y = 0.059$ pN/nm (non-rotated axes), comparable to the results from the Stoke's method.

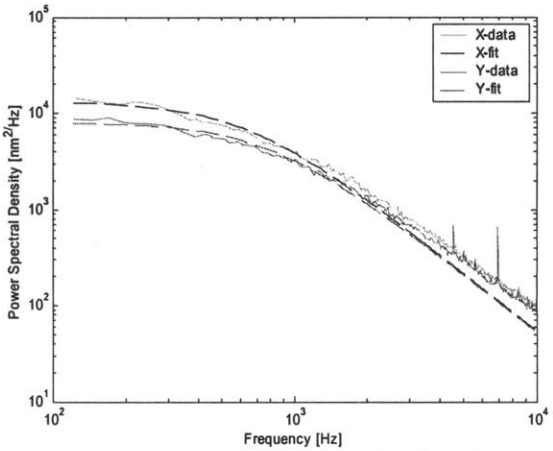

Figure 4.7. Power spectrum of bead undergoing Brownian motion while being trap. The roll-off frequency for the *x*-coordinate is 1020 Hz resulting in a trap stiffness of 0.060 pN/nm. For the *y*-axis, the roll-off frequency is 996 Hz, for a trap stiffness of 0.059 pN/nm. Data collected at 100 MHz for 6.5 seconds.

4.1.3 TIRF

The TIRF system was successfully implemented. Figure 4.8 shows several pictures comparing normal fluorescence microscopy and TIRFM. The specimen consists of actin filaments labeled with the dye Alexa-Fluor 488, which has a maximum absorption at 500nm wavelength and maximum emission at 520nm wavelength. Once the dye is excited, its emission is directed to the imaging system consisting of a telescope and a

CCD camera. The TIRF images show that the actin filaments that are close to or on the surface of the coverslip are readily visible (Figure 4.8, B), while the background is relatively dark. The other picture (Figure 4.8, A) shows a much lower contrast between actin filaments and the solution, where epifluorescence is used instead of TIRF.

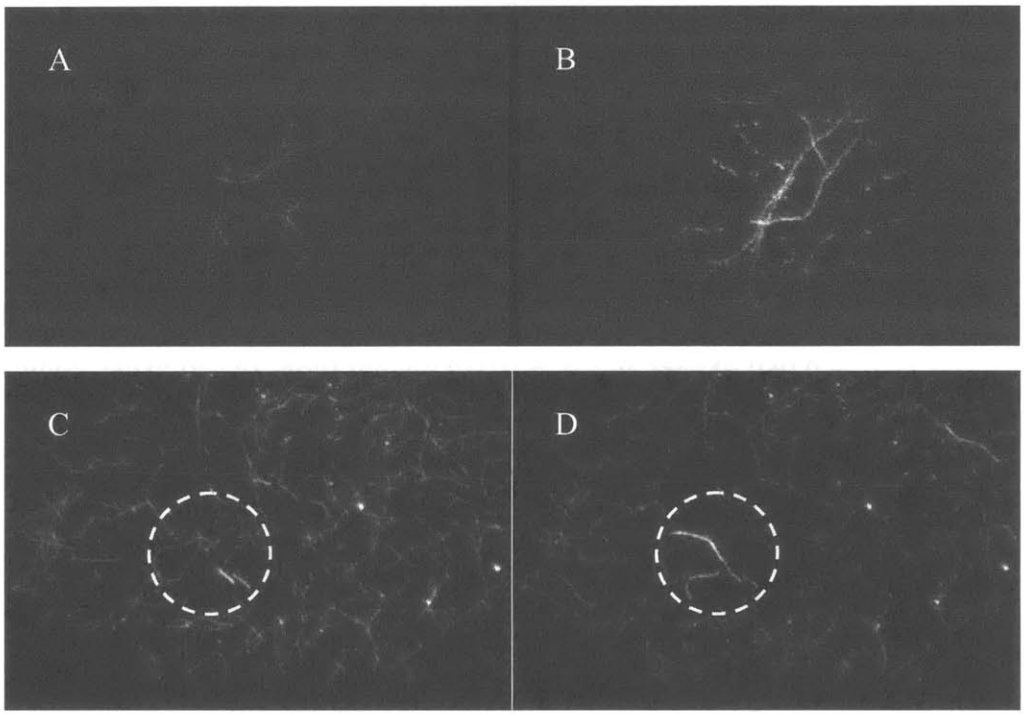

Figure 4.8. Imaging actin filaments using TIRF. *A*, epifluorescence image of actin filaments. *B*, same slide as *A* but using TIRF (same laser power as in *A*). Notice how much brighter the filaments appear, and more contrast is obtained. *C* and *D*, pictures of same area with 3 seconds difference. The dashed circle shows a region where a new actin filament lands on the surface and enters the evanescent wave. Notice in *D* the photobleacing effects are becoming evident.

4.1.4 Single Molecule Fluorescence Detection

In order to perform single molecule fluorescence microscopy it is optimal to choose a concentration so that on average, there is only one florescent molecule in the fluorescence collection volume at a time. The concentration required is described in detail in 4.3.1 below, giving a final concentration of 3.75 nM. If a higher concentration is used, then events involving multiple molecules can be monitored. For example, Figure 4.9 shows an actual photobleaching event of a single Alexa-Fluor 488 (Molecular Probes) dye molecule. Note in this figure that the step-down of the photodiode count indicate the photobleaching event for the specific molecule. This figure also shows the successful implementation of the system dedicated for single molecule fluorescence microscopy.

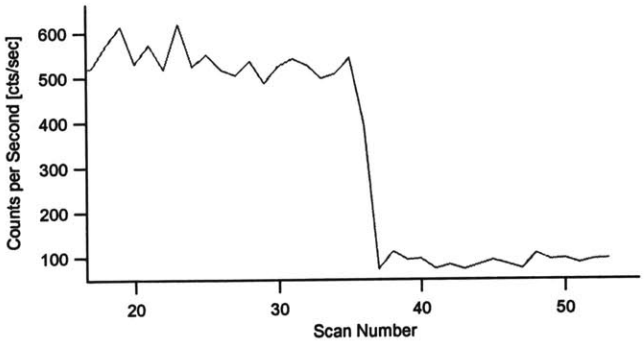

Figure 4.9. Photobleaching event of a single molecule.

4.2 Experimental Assay Results

Using the procedures described in chapter 3, the actin tether was successfully obtained. After preparing the F-actin bound to beads, three types of tethers were observed. The first type was a single filament bound to a single bead (Figure 4.10, A). The second type consisted on a single bead with multiple filaments bound (Figure 4.10, B). This type was more common than the first type. The third and less common type was beads with no filaments attached (not shown). The distribution of these types appears to come from the randomness of the myosin coverage on the bead surface, as well as variations on the concentration of actin filaments in solution. Also, free actin filaments were always observed floating in solution in all experiments.

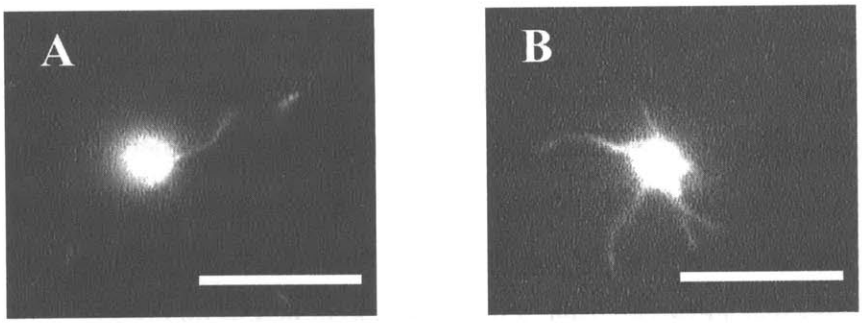

Figure 4.10. Fluorescence image of F-actin bound to myosin coated bead. *A*, single filament bound to bead; *B*, multiple filaments bound to a single bead. Scale bar: 5μm.

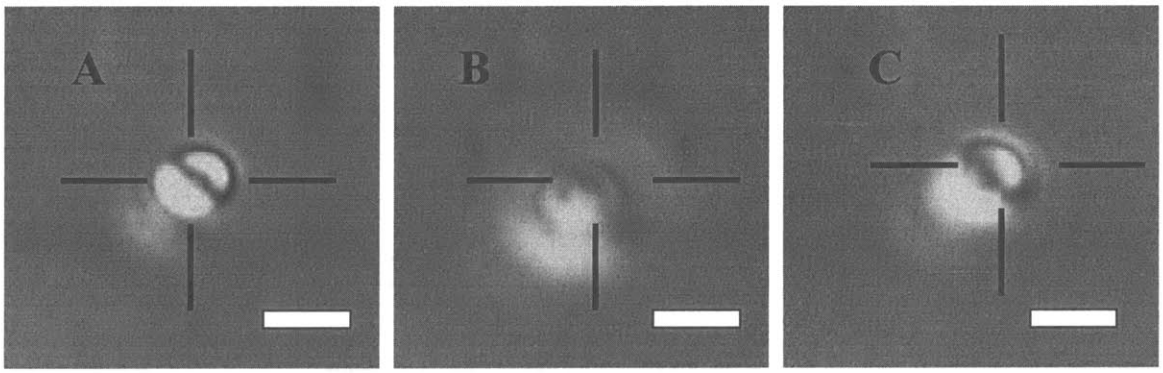

Figure 4.11. Testing an F-actin tether. Once an actin tether is observed, the fluorescent excitation is turned off and the bead is monitored using bright field. *A*, bead is centered on the trap (crosshairs). *B*, the stage is moved away from the trap until the bead gets out of focus. This is the limit of the f-actin length. *C*, the trap is moved back and the bead starts to get focused. Scale bar: 1 μm.

As described in section 3.2.1, there were two methods of obtaining the surface-actin-bead tether. The first approach, scanning the surface until a tether is found, is straightforward, but it was rarely found. On the second approach, actively constructing the tether, a free bead (with no filaments attached) was trapped, and the surface was scanned for an actin filament bound on one end to the surface and the other end free in solution. This type of filament was commonly found in the experimental assay. The bead was then rubbed against the free end of the filament until binding occurred. This technique has been used previously [41]. Next, the fluorescence excitation was turned off, and bright field illumination was used to observe the bead displacement (Figure 4.11, A). To verify that there was an actual tether, the trapped bead was moved away from the surface attachment point. Once the filament is completely stretched, further trap displacement will make the bead move out of the trap, and, therefore, out of focus since the filament pulls the bead towards the surface (Figure 4.11, B). The trap was then moved back to the original position where the bead returns to focus (Figure 4.11, C). If this behavior was observed, then a tether was assumed to be present. On the other hand, if the bead always stayed in focus with the trap, then either there was no actual tether or the linkage between one of the components was weak and broken. Also, the actual actin tethers were observed using fluorescence microscopy (data not shown).

4.3 *Theoretical Approximation of: Dissociation Rate between F-actin and APB's, and Force-Extension of F-actin*

4.3.1 Experimental Concentration of Protein and Beads

In order to record single molecule events, the concentration of α-actinin (or any other protein) in the fluorescence collection volume need to be on average a single molecule at a time. The volume of the fluorescence collection zone is given by the area projected by the pinhole on the specimen plane, times the height of the evanescent wave:

$$V_{exc} = A_{pinhole} \cdot h_{wave} \approx \frac{\pi\left(1.5\times10^{-6}\,\mathrm{m}\right)^2}{4} \cdot \left(250\times10^{-9}\,\mathrm{m}\right) = 4.42\times10^{-19}\,\mathrm{m}^3 \quad \text{Equation 4.1}$$

Since the number of molecules per mol of substance is given by Avogadro's number (N_{av}), the concentration, $[C]_{APB}$, required for single molecule detection is given by

$$[C]_{APB} = \frac{1 molecule}{N_{av} \cdot V_{exc}} = \frac{1 molecule}{\left(6.022\times10^{23}\, molecules/mol\right) \cdot 4.42\times10^{-16}\,\mathrm{L}} = 3.75\mathrm{nM}. \quad \text{Equation 4.2}$$

In the same way, for experiments using proteins bound to beads, it is required to have just one bead on the collection zone. The concentration of beads required is

$$[C]_{bead} = \frac{1 bead}{V_{exc}} = \frac{1}{4.42\times10^{-16}\,\mathrm{L}} = 2.26\times10^{15}\,\frac{beads}{\mathrm{L}} = 2.26\times10^{12}\,\frac{beads}{\mathrm{mL}}. \quad \text{Equation 4.3}$$

The concentrations $[C]_{APB}$ and $[C]_{bead}$ will be used when introducing the actin binding proteins to the experimental assay.

4.3.2 Selection of Bead Size for ABP's

For the experiments described in chapter 3, there are two timescales of interest: the protein unbinding timescale, and the diffusion timescale. Because the interest of this research is to determine the unbinding rate of ABP's with actin, it is required that these two timescales must be different from each other. The characteristic timescales for these two processes are described in Equation 4.4 and Equation 4.5 respectively:

$$\tau_{bind} \sim k_{off}^{-1}, \quad \text{Equation 4.4}$$

$$\tau_{diff} \sim \frac{l^2}{D}, \quad \text{Equation 4.5}$$

Where τ_{bind} is the characteristic binding event duration, l is the end-to-end distance of the bead displacement during diffusion and D is the diffusivity of the bead given by the Stokes-Einstein equation,

$$D = \frac{k_B T}{6\pi\mu a}. \qquad \text{Equation 4.6}$$

In this last equation $k_B T$ is the thermal energy, μ is the fluid viscosity and a is the bead radius. Combining Equation 4.5 and Equation 4.6, the diffusion timescale can be approximated as a function of the bead radius:

$$\tau_{diff}(a) \approx \frac{6\pi\mu l^2}{k_B T} a. \qquad \text{Equation 4.7}$$

For the experimental setup, the diffusion distance consists of the diagonal across the excitation zone plus twice the radius of the bead, since the photodetectors will receive signals once a portion of the bead enters the excitation zone. Because the diameter of the excitation zone is much larger than its height (d » h), the diffusion distance as a function of bead radius can be approximated as

$$l(a) \approx d + 2a \qquad \text{Equation 4.8}$$

where d is the diameter of the excitation zone. Combining this equation with Equation 4.7, the diffusion timescale becomes

$$\tau_{diff}(a) \approx \frac{6\pi\mu(d+2a)^2}{k_B T} a. \qquad \text{Equation 4.9}$$

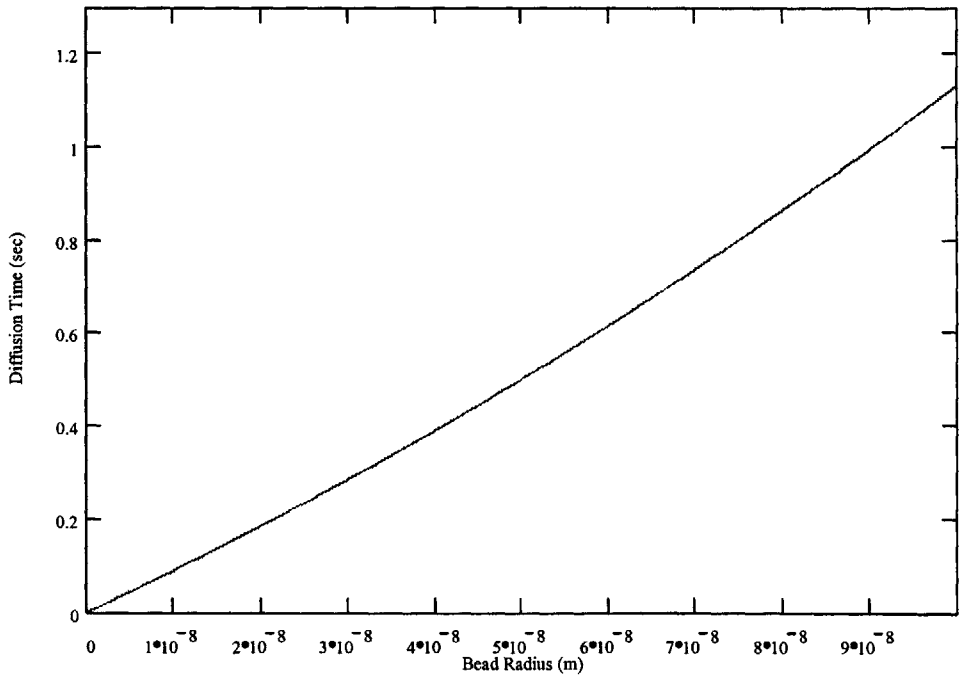

Figure 4.12. Diffusion time as a function of bead radius for a bead to cross the excitation zone.

The function described in Equation 4.9 is plotted in Figure 4.12 for conditions at room temperature (T =300 K, μ = 1 cp), and a pinhole diameter of 1.5 μm. From the literature [44], the dissociation rate between actin and α-actinin is ~ 0.4 sec^{-1}, which gives a τ_{bind} ~ 2.5 sec. By selecting a bead with a radius of 20 nm, the estimated diffusion time is ~ 0.2 sec, or one order of magnitude less than the unbinding time scale. This difference is expected to be large enough to distinguish between diffusion and binding events.

During actual experiments, the diffusion timescale represents the lower bound for the resolution of the binding event duration. Therefore, data recorded by the photodetectors that have a signal duration equal or less than the diffusion time, are considered ambiguous and must be discarded. In the following section, a simulation of the expected data is presented and analyzed to demonstrate how the unbinding rate constant can be obtained.

4.3.3 Data Simulation

Here, a simulation based on the dissociation rate between α-actinin and actin (k_{off}) generated the expected experimental data collection by the photodiode. The conditions were assumed to be at room temperature and in aqueous solution. The model simulates a protein bound to a fluorescent bead with a 20 nm radius, and no force applied. It is also assumed that binding events are governed by first order kinetics. The data collected for one thousand binding events is simulated by a random number generator from an exponential distribution with mean of k_{off}(0.4 sec^{-1} with no force, [44]). The raw data are shown in Figure 4.13 (A). The data are then truncated by the lower time limit given by the diffusion time for the given bead size, which is 0.186 seconds (Figure 4.13, B). Note that the number of reportable binding events is reduced by around 16%.

The truncated data are plotted in a histogram normalized by the width of each bin. The data are then fitted to a scaled exponential probability distribution [32] in the form of

$$\frac{n_i}{\Delta t_{bin,i}} = \frac{N}{\tau}\exp\left(\frac{t_{\min} - t_{mid,i}}{\tau}\right). \qquad \text{Equation 4.10}$$

where n_i is the number of events on the bin i, $\Delta t_{bin,i}$ is the width of the bin i, N is the total number of events (after data truncation), t_{min} is the lower time limit (or τ_{diff}), $t_{mid,i}$ is the event duration corresponding to the center of the bin i, and τ is the decay time constant,

which is equal to the inverse of k_{off}. For this simulation, the data are distributed among twenty bins of equal width. The bin width is determined by

$$\Delta t_{bin} = \frac{t_{\max} - t_{\min}}{\#\ of\ bins} \qquad \text{Equation 4.11}$$

where t_{max} is the longest event duration recorded by the photodiode. The data histogram and the fit are shown in Figure 4.14. The simulation generated a dissociation rate to 0.412 ± 0.024 sec^{-1} (95% confidence) compared to the reported value of 0.4 sec^{-1}. This result shows that if the data obtained from experimental procedures come from an exponential probability distribution, a dissociation rate can be obtained. During experiments, this same procedure will be used to analyze the data while the force applied to the actin filament is varied.

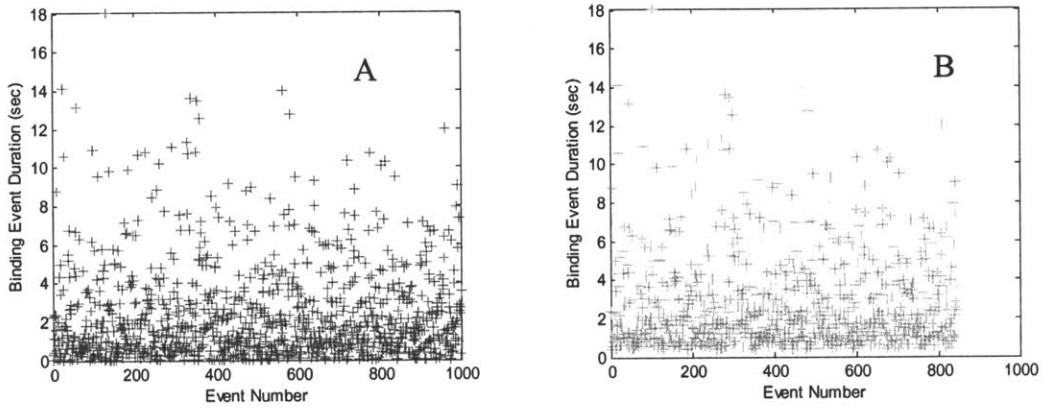

Figure 4.13. Experimental simulation of 1000 events. A, simulation of raw data recorded by the photodector. The horizontal axis shows the event number and its corresponding time duration of the binding event is shown in the vertical axis. B, data from A is truncated by the diffusion time (i.e. events with duration less than 0.186 s) and replotted. Note that the "effective" number of binding events is reduced to 846 events.

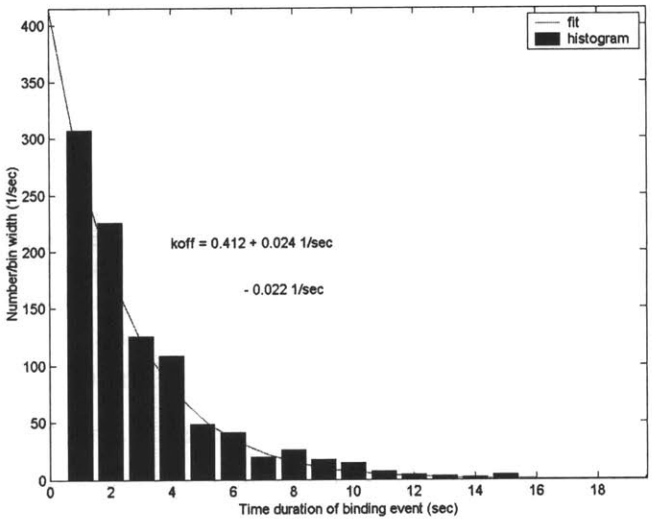

Figure 4.14. Histogram of binding duration time and fitted exponential distribution (n = 846).

4.3.4 Extension of F-actin

The filament-bead system can be modeled as two spring in series as shown in Figure 4.15. The actin filament is characterized as a Hookean spring with constant k, and the trap is represented by the stiffness α. The bead represents the link between the two springs. The displacement Δu_{trap} represents the displacement of the bead relative to the center of the trap, and Δu_{actin} represents the stretching length of the filament. The force-displacement for each spring is described by

$$F_{trap} = \alpha \Delta u_{trap} \qquad \text{Equation 4.12}$$

$$F_{actin} = k \Delta u_{actin} \qquad \text{Equation 4.13}$$

A force balance at the junction between the two springs has the following result:

$$F_{trap} = F_{actin}. \qquad \text{Equation 4.14}$$

Combining these last three equations, the amount of stretching of the actin filament is given by

$$\Delta u_{actin} = \frac{\alpha \Delta u_{trap}}{k}. \qquad \text{Equation 4.15}$$

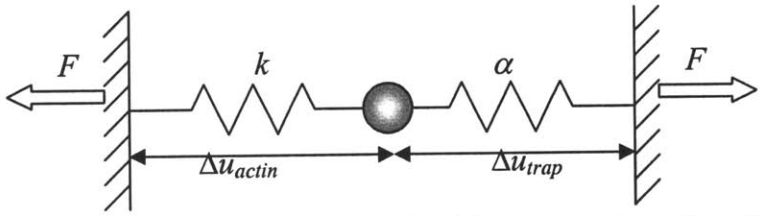

Figure 4.15. Schematic representation of actin-bead-trap system. The actin filament and the optical trap are characterized as a Hookean springs with constant k and α respectively. Both springs are coupled together by the bead (sphere). When a force F is applied, the bead is displaced from the center of the trap (Δu_{trap}), generating a displacement on the filament (Δu_{actin})

In general, the properties of materials are given in terms of force normalized by the active area (Young's modulus) instead of spring constant. Using this approach, the force-displacement relationship can be written in terms of stress-strain (in one dimension)

$$\sigma = \frac{F}{A} = E\varepsilon, \qquad \text{Equation 4.16}$$

$$\varepsilon = \frac{\Delta L}{L} \qquad \text{Equation 4.17}$$

where σ is the normal stress, A is the normal area, E is the Young's modulus and ε is the strain, and L is the original length of the specimen. Combining Equation 4.16 and Equation 4.17, the spring constant can be expressed in terms of Young's modulus, the original length and the normal area:

$$k = \frac{F}{\Delta L} = \frac{(F/A)A}{(\Delta L/L)L} = \frac{\sigma A}{\varepsilon L} = \frac{EA}{L} \qquad \text{Equation 4.18}$$

Assuming a filament diameter of 7 nm [45], a Young's modulus of 2.2 GPa [46], and a filament length of ~ 10 μm, the effective spring constant for such filament is ~ 7.7 pN/nm. Using this result, combined with Equation 4.15, the expected filament extension can be estimated for experimental procedures.

Chapter 5: Discussion

Equipment development

As described in chapter 2, the equipment was designed for accuracy and stability. All the additions to the microscope were designed with small shape factor (length/width ~1) to minimize vibrations induced by structural instabilities, air currents, and accidental bumps. One of the most difficult challenges for the design was the space limitation. All the additional parts had to fit in the space that the original parts once occupied, plus some clearance was required for the movable parts, like the TIRF system. This required several design iterations before the design was finalized. Also, to keep the machining costs affordable, the design of each part was kept as simple as possible, avoiding small features and complex geometries. Once assembled, the instrument showed to be a robust design in general. The only part that appears to be sensitive to vibrations is the detection branch, since it is attached to the condenser as a cantilever with a relatively long arm. This design was the outcome of critical space limitations. Although position detection experiments appear to be repeatable and basically unaffected by this cantilever, a second design is under consideration that would replace the cantilever arm with a rigid support to hold the detection branch and all the associated optics and electronics.

Position detection

As shown in Figure 4.3, the detection system can record displacements as small as 5 nm. For molecular interactions, this is the characteristic length scale for protein conformation changes. It is also in the same order of magnitude of the kinesin molecular motors steps (~ 8nm [31]), and about 10 times smaller than the myosin V steps (~ 40 nm [47]) along an actin filament. Also, the detection range for the system consists of a circular area with a diameter of about 200 nm; therefore, the maximum displacement that a bead can be displaced from the center of the trap within the calibration zone is 100 nm. This also determines the limit of the force that can be applied for a given trap stiffness, according to Equation 4.12. To increase the position resolution of the system, other models of photodiodes with a larger active area are being considered, in combination of image magnification. This type of arrangement is expected to improve the resolution to a

one nanometer range. Also reducing acoustical noise, and improving laser and optics stability should also help enhance the position detection.

Trap stiffness and actin extension

The fluid mechanics and statistical mechanics methods agreed very well in the calculation of the trap stiffness. However, the statistical mechanics method showed that the trap profile is not symmetric with respect to its origin, having an elliptical shape instead of a circular one. This asymmetry gives rise to uneven forces in the two orthogonal directions, which is evident from Figure 4.5. The source of the asymmetry can be the result of beam misalignment, optical aberrations, and beam polarization. If the beam entering the objective is not parallel with the microscope optical axis, then when exiting the objective the angular misalignment is amplified. Consequently, even if the beam cross-section is circular, it will appear elliptical relative the specimen plane. To solve this problem, the optical path has to be corrected.

For many optical components (lenses, mirrors, etc), physical aberrations are minimized at the center of the component. If the beam enters the optics somewhat far from the center, aberrations at the output beam could change its orientation, efficiency and mode. As for the first problem, this is corrected by careful inspection of the location of the beam relative to the center of all the optics along the optical path.

Generally, optical traps can generate forces in the 100 pN range. Therefore, if such force is applied to an actin filament with spring constant ~ 7 pN/nm (see section 4.3.4), the extension of the filament would be about 14 nm. In order to generate such force, using a trap stiffness of ~ 0.05 pN/nm (see section 4.1.2), the bead displacement has to be ~ 2 μm, which is physically impossible since the bead will fall out of the trap when the displacement is ~ 200 nm. This result shows that instrument needs to be optimized in order to get trap stiffness in the order of 1 pN/nm.

To increase the trap stiffness, the beam has to be completely aligned with the microscope optical axis and aberrations form optical components have to be minimized as described above. Other methods of improving the trap stiffness are both increasing the bead size (Equation 3.7) and increasing the power output from the laser head. Careful consideration has to be in mind when increasing the power output of the laser because

excesses power could damage some of the optics along the beam path, as well as it presents a hazardous condition to the human eye.

Biological assays

Preliminary results showed that an actin filament tether was obtained. In addition, the bead at the end of the tether was trapped and manipulated without breaking the attachment between the filament and the surface or between the filament and the bead. Also, the single molecule detection system proved to be successful. From the results in section 4.3, by introducing actin binding proteins at a concentration of 3.75 nM to the actin assay, single molecule binding events should be recorded. From statistical analysis of the results, an estimate of the dissociation constant can be computed, assuming that the interaction is governed by first order kinetics. This approximation also assumes that there are no other interactions in solution and there is no binding hindrance.

By applying a tensile force to the actin filament, the energy landscape of the reaction should be shifted, but the direction of the shift is not known, that is, increasing force can either increase or reduce the dissociation rate. For example, if a binding pocket is partially closed under no force, then applying force could open the binding site providing a tighter interaction between the molecules, decreasing the dissociation rate. On the other hand, if a binding site is at its optimal state under no force, applying a force could stretch the binding pocket, reducing the effective contact area between molecules, increasing the dissociation rate. The force-dissociation rate relationship is expected to vary between the actin binding proteins, where some will have a positive relationship while others have a negative. As a result, the effect of the force on the molecular interactions in this case is quite unpredictable.

Chapter 6: Conclusions and Future Directions

To complete the experimental procedures, there is still some more work to be done. This work includes: completing the actual experiments with α-actinin and other actin binding proteins, implementing microfluidics to provide better control over delivery of reagents, and developing molecular simulations based on experimental results. Also, a technique for tri-dimensional optical trapping is being developed to improve experimental capabilities over other existing optical traps.

Experiments and Computational Simulations

The next step for the experiments is to actually introduce actin binding proteins into the assay containing the actin tether and monitor the binding events as described in section 3.2.2. The initial target protein is α-actinin. Once the setup is completed and validated other actin binding proteins of interest (Table 1.1) will be tested. By studying the interactions between actin and different proteins, a better understanding of the signaling cascade that transduces force into a biological reaction can be obtained.

The results of these experiments can be used to build computational models that simulate the molecular interactions of actin and ABP's. From these models, different physiological conditions can be simulated in order to make predictions of the bio-chemical behavior of proteins. Also, these models can be coupled to models that simulate the force transduction signaling cascade in order to obtain a more thorough understanding of how forces affect cell migration, proliferation and survival.

Microfluidics

The development of microfluidics for biological applications is a fast growing field. By using a highly controlled laminar flow, researchers are using microfluidics channels for DNA analysis [48, 49], cell manipulation and separation [50, 51], biomolecular detection [52] and others. To take advantage of the microfluidics technology, a channel will be developed in order to provide a fast, reliable and reproducible delivery of reagents for the experimental procedures presented here. For example, a channel with three inlets and one outlet can be very useful for this application. One inlet can deliver the myosin solution to coat the surface of the channel. Through the second inlet, the BSA solution can be introduced to remove the excess myosin, and the third inlet would deliver the

solution containing the actin filaments and the myosin coated beads. The outlet would send all the reagents to a reservoir for future disposal. A preliminary design for the channel has been developed but it needs to be made and tested before its implementation to the experimental set up.

3-D Trapping Manipulation

Currently, there are different techniques to manipulate the laser trap in the specimen plane: steering mirrors, acousto-optical devices (AOD), and holographic diffractive optics[53]. Using steering mirrors and AOD's provide fast control of the laser in a plane but no 3D manipulation is attainable. On the other hand, holographic diffractive optics provides some 3D control over the optical trap but it has some limitations. First, its resolution is about 20 nm compared to 5 nm using AOD's. Second, the generation of the diffractive hologram is a highly computational process; therefore, it reduces the response time of the system. This system is also expensive and bulky. Here, a new method is described to obtain fast, reliable and automated positioning of the trap in 3-dimensions by using a compact piezo stage (Nanocube P-611.3S; Polytech PI).

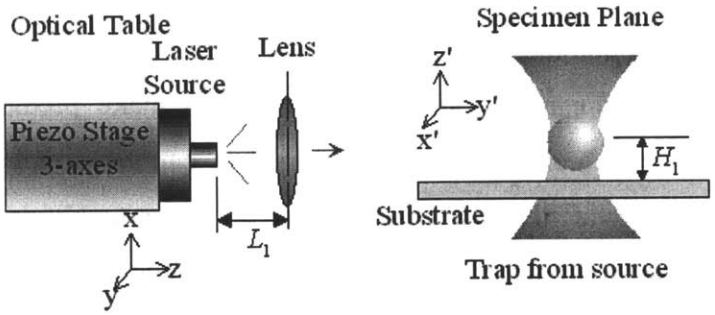

Figure 6.1. Experimental setup for 3-dimensional control of optical trap location. The laser output is mounted on a 3-axes piezo-stage, which moves relative to a collimating lens. The result is a controllable laser focus location on the specimen plane.

By mounting the output fiber of a laser source onto a nano-positioning device, coupled with a collimating lens, 3-dimensional control of the trap could be achieved. The proposed setup is depicted in Figure 6.1. The laser beam goes through a collimating lens at a distance L_1 and other optical elements into a microscope, where the beam is focused at an arbitrary height H_1 above the specimen plane. By moving the laser source in a plane parallel to the lens (x-y plane), the focus of the beam will move parallel to the specimen plane (x'-y' plane), but will remain at the same height H_1. But if the distance (L_1) between

the laser source and the lens is decreased (or increased), the height of the trap focus will increase (or decrease) giving the height control of the focus that other systems are not capable of accomplishing. In summary, a change in position of the laser source (ΔR_s) relative to the lens will result in a change of position of the focus (ΔR_f) of the trap at the specimen plane. The relation between ΔR_s and ΔR_f depends on the optical elements between the laser source and the experimental sample, and will be determined empirically by analyzing experimental results. In this way, a precise calibration curve between source position and trap position can be obtained.

Closing remarks

In this work, the design and construction of an instrument to study the mechanics of a single actin filament at different force levels was presented. The instrument consists of an optical trap combined with single molecule fluorescence. Initial results show that the instrument is capable of trapping particles and manipulate them with a resolution in the nanometer scale. However, the stiffness of the trap is quite low. Further work has to be done to optimize the stiffness of the trap and the efficiency of the instrument. On the other hand, the single molecule detection system was successfully demonstrated by recording a photobleaching event of a single chromophore molecule. In general, after some optimization, the instrument will be ready to use for recording single molecule binding events between an actin filament and actin binding proteins.

Another aspect presented here was the preparation of the biological assays. A protocol to tether a single actin filament from the surface to a bead was successfully developed and implemented. Preliminary results show that by trapping the tethered bead and moving it away from the surface attachment point, the actin filament can be held taut, and forces can be applied to it. This consists of only one portion of the overall research goal. The next portion consists of introducing the actin binding proteins into the assay and record binding events to determine the kinetic dissociation rate as a function of applied force. The theoretical methods on how to determine the dissociation constant was also presented based on previous work.

The actin protein is one of the major components in the cytoplasm of most eukaryotic cells. From the thousands of proteins inside the cell, it comprises for about 5% of the

total protein count. This protein plays important roles in cell migration, adhesion, force transmission, and muscle contraction, which are all mechanical processes. Understanding how the mechanics of actin filaments affect the bio-chemical behavior of the cell is therefore an important field of study. For example, during metastasis, cancerous cells migrate from their original site into the blood stream in order to spread to different organs. If the binding kinetics between a certain protein and actin is known, a possible treatment is to target that protein such that it becomes inactive under certain force conditions that promote cell migration. In atherosclerosis, the endothelial cells in the arterial walls become thickened and rigid, especially in arterial bifurcations where shear stresses are low and cyclical. These observations suggest that there is a force dependency on development of the disease. One step in the direction of comprehending how different levels of shear forces affect the cell behavior is to study how different levels of forces affect the behavior of one of the major components of the cytoskeleton: actin.

I want to thank my two advisors Roger D. Kamm and Matthew J. Lang for providing me the opportunity to work with them. They are a great source for technical background in their field of study as well as excellent personal motivators. Without their support and encouragement this work would not have been a success. I also want to acknowledge the lab members from the Kamm Lab and the Lang Lab. Their continuous feedback pointed my research into the right direction. Special thanks go to Ricardo Brau, Peter Lee, David Appleyard and Jenny Ta. Their help was critical for the completion of the design and construction of the experimental equipment.

Unique thanks go to my wife Janice. Her constant support and patience were a source of motivation for completing this work.

References

1. Lang, M.J., P.M. Fordyce, and S.M. Block, *Combined optical trapping and single-molecule fluorescence.* J Biology, 2003. **2**: p. 6.1-6.4.
2. Satcher, R., C.F. Dewey, Jr., and J.H. Hartwig, *Mechanical remodeling of endothelial surface and actin cytoskeleton induced by fluid flow.* Microcirculation, 1997. **4**: p. 439-453.
3. McGrath, J.L., J.H. Hartwig, Y. Tardy, and C.F. Dewey, Jr., *Measuring actin dynamics in endothelial cells.* Microsc Res Tech, 1998. **43**(5): p. 385-94.
4. Small, J.V., T. Stradal, E. Vignal, and K. Rottner, *The lamellipodium: where motility begins.* Trends Cell Biol, 2002. **12**(3): p. 112-20.
5. Pantaloni, D., C. Le Clainche, and M.F. Carlier, *Mechanism of actin-based motility.* Science, 2001. **292**(5521): p. 1502-6.
6. Pollard, T.D. and G.G. Borisy, *Cellular motility driven by assembly and disassembly of actin filaments.* Cell, 2003. **112**(4): p. 453-65.
7. Maheshwari, G. and D.A. Lauffenburger, *Deconstructing (and reconstructing) cell migration.* Microsc Res Tech, 1998. **43**(5): p. 358-68.
8. Danuser, G. and R. Oldenbourg, *Probing f-actin flow by tracking shape fluctuations of radial bundles in lamellipodia of motile cells.* Biophys J, 2000. **79**(1): p. 191-201.
9. Choquet, D., D.P. Felsenfeld, and M.P. Sheetz, *Extracellular matrix rigidity causes strengthening of integrin-cytoskeletal linkages.* Cell, 1997. **88**: p. 39-48.
10. Critchley, D.R., *Focal adhesions - the cytoskeletal connection.* Curr Opin Cell Biol, 2000. **12**: p. 133-139.
11. Oosawa, F., *A historical perspective of actin assembly and its interactions*, in *Molecular Interactions of Actin*, C.G. dos Remedios and D.D. Thomas, Editors. 2001, Springer: Berlin. p. 9-21.
12. Sawada, Y. and M.P. Sheetz, *Force transduction by Triton cytoskeletons.* J Cell Biol, 2002. **156**(4): p. 609-615.
13. Lebedev, P.N., *Experimental examination of light pressure.* Ann. der Physik, 1901. **6**: p. 433-459.
14. Nichols, E.F. and G.F. Hull, *A preliminary communication on the pressure of heat and radiation pressure.* Phys Rev, 1901. **13**: p. 307-308, 317-320.
15. Ashkin, A., *Acceleration and trapping of particles by radiation pressure.* Phys Rev Letter, 1970. **24**: p. 154-159.
16. Ashkin, A., *Optical levitation by radiation pressure.* Appl Phys Lett, 1971. **19**: p. 283-285.
17. Ashkin, A., *Applications of laser radiation pressure.* Science, 1980. **210**: p. 1081-1088.
18. Ashkin, A., *Forces of a single-beam gradient laser trap on a dielectric sphere in the ray optics regime.* Biophys J, 1992. **61**: p. 569-582.
19. Ashkin, A., J. Dziedzic, J. Bjorkholm, and S. Chu, *Observation of a single gradient force optical trap for dielectric particles.* Opt Lett, 1986. **11**: p. 288-290.
20. Ashkin, A., J. Dziedzic, and J. Bjorkholm, *Optical trapping and manipulation of single cells using infrared laser beams.* Nature, 1987. **330**: p. 769-771.
21. Ashkin, A. and J. Dziedzic, *Optical trapping and manipulation of viruses and bacteria.* Science, 1987. **235**: p. 1517-1520.

22. Lenormand, G., S. Henon, A. Richert, J. Simeon, and F. Gallet, *Direct measurement of the area expansion and shear moduli of the human red blood cell membrane skeleton.* Biophys J, 2001. **81**(1): p. 43-56.
23. Dao, M., C.T. Lim, and S. Suresh, *Mechanics of the human red blood cell deformed by optical tweezers.* J Mech Phys Solids, 2003. **51**: p. 2259-2280.
24. Giannone, G., B.J. Dubin-Thaler, H. Dobereiner, N. Kieffer, A.R. Bresnick, and M.P. Sheetz, *Periodic lamellipodial contractions correlate with rearward actin waves.* Cell, 2004. **116**: p. 431-443.
25. Raucher, D. and M.P. Sheetz, *Cell spreading and lamellipodial extension rate is regulated by membrane extension.* J Cell Biol, 2000. **148**(1): p. 127-136.
26. Galbraith, C.G., K. Yamada, and M.P. Sheetz, *The relationship between force and focal complex development.* J Cell Biol, 2002. **159**(4): p. 695-705.
27. Wright, W.H., G.J. Sonek, Y. Tadir, and M.W. Berns, *Laser trapping in cell biology.* IEEE J Quantum Electron, 1990. **26**(12): p. 2148-2157.
28. Wang, M.D., H. Yin, R. Landick, J. Gelles, and S.M. Block, *Stretching DNA with optical tweezers.* Biophys J, 1997. **72**(1335-1346).
29. Perkins, T.T., S.R. Quake, D.E. Smith, and S. Chu, *Relaxation of a single DNA molecule observed by optical microscopy.* Science, 1994. **264**: p. 822-826.
30. Block, S.M., L.S. Goldstein, and B.J. Schnapp, *Bead movement by single kinesin molecules studied with optical tweezers.* Nature, 1990. **348**(348-352).
31. Lang, M.J., C.L. Asbury, J.W. Shaevitz, and S.M. Block, *An automated two-dimensional optical force clamp for single molecule studies.* Biophys J, 2002. **83**(1): p. 491-501.
32. Veugmeyster, Y., E. Berliner, and H. Gelles, *Release of Isolated Single Kinesin Molecules from Microtubules.* Biochemistry, 1998. **37**: p. 747-757.
33. Yasuda, R., H. Miyata, and J. Kinosita, K., *Direct measurement of the torsional rigidity of single actin filaments.* J Mol Biol, 1996. **263**(3): p. 227-236.
34. Simmons, R.M., J.T. Finer, H.M. Warrick, B. Kralik, S. Chu, and J.A. Spudich, *Force on single actin filaments in a motility assay measured with an optical trap.* Adv Exp Med Biol, 1993. **332**: p. 331-336.
35. Finer, J.T., R.M. Simmons, and J.A. Spudich, *Single myosin molecule mechanics: piconewton forces and nanometer steps.* Nature, 1994. **368**: p. 113-119.
36. Svoboda, K. and S.M. Block, *Biological applications of optical forces.* Annu Rev Biophys Biomol Struct, 1994. **23**: p. 247-85.
37. Lang, M.J. and S.M. Block, *Resource letter: LBOT-1: Laser-based optical tweezers.* Am J Phys, 2003. **71**(2): p. 201-215.
38. Visscher, K., S.P. Gross, and S.M. Block, *Construction of multiple-beam optical traps with nanometer-resolution position sensing.* IEEE J Quantum Electron, 1996. **2**(4): p. 1066-1076.
39. Gittes, F. and C.F. Schmidt, *Interference model for back-focal-plane displacement detection in optical tweezers.* Optical Society of America, 1998. **23**(1): p. 7-9.
40. Berg-Sorensen, K. and H. Flyvbjerg, *Power spectrum analysis for optical tweezers.* Rev Sci Instr, 2004. **75**(3): p. 594-612.
41. Dupuis, D.E., W.H. Guilford, and D.M. Warshaw, *Actin filaments mechanics in the laser trap.* J Muscle Res Cell Mot, 1997. **18**: p. 17-30.

42. Suzuki, N., H. Miyata, S. Ishiwata, and J. Kinosita, K., *Preparation of bead-tailed actin filaments: estimation of the torque produced by the sliding force in an in vitro motility assay.* Biophys J, 1996. **70**: p. 401-408.
43. Miyata, H., R. Yasuda, and K.K. Jr., *Strength and lifetime of the bond between actin and skeletal muscle alpha-actinin studied with an optical trapping technique.* Biochimica et Biophysica Acta, 1996. **1290**: p. 83-88.
44. Goldmann, W.H. and G. Isenberg, *Analysis of filamin and alpha-actinin binding to actin by the stopped flow method.* FEBS, 1993. **336**: p. 408-410.
45. Lodish, H., A. Berk, P. Matsudaira, C.A. Kaiser, M. Krieger, M.P. Scott, S.L. Zipursky, and J. Darnell, *Molecular Cell Biology*. Fifth ed. 2004, New York: W.H. Freeman and Company.
46. Fung, Y.C., *Mechanical Properties of Living Tissues*. second ed. Biomechanics. 1993, New York: Springer.
47. Rock, R., S.E. Rice, A.L. Wells, T.J. Purcell, J.A. Spudich, and H.L. Sweeney, *Myosin VI is a processive motor with a large step size.* PNAS, 2001. **98**(24): p. 13655-13659.
48. Lee, G.B., S.H. Chem, G.R. Huang, W.C. Sung, and Y.H. Lin, *Microfabricated plastic chips by hot embossing methods and their applications for DNA separation and detection.* Sensors and Actuators B-Chem, 2001. **75**(142-148).
49. Legally, E.T., I. Medintz, and R.A. Mathies, *Single-molecule DNA amplification and analysis in an integrated microfluidic device.* Anal Chem, 2001. **73**: p. 565-570.
50. Yang, J., Y. Huang, X.B. Wang, F.F. Becker, and P.R. Gascoyne, *Cell separation on microfabricated electrodes using dielectrophoretic/graviational field flow fractionation.* Anal Chem, 1999. **71**: p. 911-918.
51. Glasgow, I.K., H.C. Zeringue, D.J. Beebe, S.-J. Choi, J.T. Lyman, N.G. Chan, and M.B. Wheeler, *Handling individual mammalian embryos using microfluidics.* IEEE Trans Biomed Eng, 2001. **48**(5): p. 570-578.
52. Burg, T.P. and S.R. Manalis, *Suspended microchannel resonator for biomolecular detection.* Appl Phys Lett, 2003. **83**(13): p. 2698-2700.
53. Grier, D.G., *A revolution in optical manipulation.* Nature, 2003. **424**: p. 810-816.